Key Points:

- The relative humidity and high cloud fraction both decrease with increasing vertical resolution in System for Atmospheric Modeling
- Vertical resolution impacts convective aggregation occurrence, onset time, and equilibrium intensity
- The sensitivity of convective aggregation to domain size may depend on vertical resolution

Correspondence to:
A. M. Jenney,
andrea.jenney@oregonstate.edu

Vertical Resolution Impacts Explicit Simulation of Deep Convection

A. M. Jenney[1,2] , **S. L. Ferretti[1]** , and **M. S. Pritchard[1,3]**

[1]Department of Earth System Science, University of California, Irvine, Irvine, CA, USA, [2]College of Earth, Ocean, and Atmospheric Sciences, Oregon State University, Corvallis, OR, USA, [3]NVIDIA Research, Santa Clara, CA, USA

Abstract The aggregation of tropical convection greatly influences the mean-state of the atmosphere, altering humidity distributions, total atmospheric radiative cooling, and cloud amounts. Although studies have demonstrated the sensitivity of convective aggregation to horizontal resolution and domain size, few studies have explored the impact of *vertical* resolution on convective aggregation. Here, we investigate the impact of vertical resolution on simulations of deep convection and convective aggregation using the System for Atmospheric Modeling convection resolving model. We analyze simulations of tropical radiative-convective equilibrium with varying vertical levels (32, 64, 128, and 256) across small (100 km), medium (700 km) and large (1,500 km) domains. We demonstrate that relative humidity and cloud fraction decrease with increasing vertical resolution as a result of reduced turbulent mixing. Vertical resolution also influences the occurrence of, onset time, and equilibrium intensity of aggregated convection, and also appears to affect the sensitivity of convective aggregation to domain size. Understanding how simulated convection aggregates, as well as its simulated sensitivity to model formulation, is critical for making and interpreting future predictions of global climate change.

Plain Language Summary We study the simulation of clouds and storms in simple computer models of the tropical atmosphere. These models calculate air movement on a grid. Large grid boxes result in a very coarse, pixelated representation of the atmosphere, while smaller grid boxes offer a much clearer, high-resolution video. Ideally, the average air movement, cloud formation, and rainfall simulated by these models shouldn't be affected by the size of the grid boxes, with smaller boxes just providing additional detail. However, here we show that the height of grid boxes influences average properties of the simulations, such as the total cloud amount, the amount of rain that falls, and the relative humidity.

1. Introduction

Simulations of deep convection with convection resolving models (CRMs) are useful for understanding physical processes and mechanisms involved with precipitation and convective-scale atmospheric motions, including the generation and maintenance of organized tropical convection. Due to their ability to resolve convective-scale turbulent motions, CRMs remain popular tools used to inform convective parameterizations (e.g., Wang et al., 2022).

In simulations of radiative-convective equilibrium, both with large limited-domain CRMs and Earth-sized global circulation models (GCMs), there is a tendency for convection to organize into one or multiple large clusters (reviewed in Wing et al., 2017). This behavior is referred to as convective aggregation. When convection transitions from spatially disorganized to an aggregated state, the tropospheric humidity distribution widens and total atmospheric radiative cooling increases (e.g., Wing & Emanuel, 2014), and simulated high cloud amount decreases while low cloud amount increases (Wing & Cronin, 2016). Observations also reveal frequent organization of tropical convection on Earth (e.g., Tobin et al., 2012). Therefore, understanding the mechanisms involved in simulating convective aggregation may improve understanding of the processes governing its variability in the real world. Furthermore, understanding both the triggering and maintenance of convective aggregation, as well as its simulated sensitivity to model formulation, is critical for making and interpreting future predictions of global climate change.

Simulated convective aggregation is sensitive to both horizontal resolution and domain size. Typically, convection only aggregates in domains larger than 200 km, and more readily when horizontal grid spacing exceeds 2 km (Muller & Held, 2012; Yanase et al., 2020). This is because simulated convective aggregation requires a net export of moist static energy from dry regions into convecting regions, which is facilitated by low-level

circulations driven by strong radiative cooling from low clouds in dry columns (e.g., Bretherton et al., 2005; Coppin & Bony, 2015; Muller & Bony, 2015; Muller & Held, 2012; Yanase et al., 2020). Larger domains permit stronger upgradient circulations, which counteract boundary layer moisture homogenization by cold pools (Jeevanjee & Romps, 2013; Yanase et al., 2020). Coarser horizontal resolution generally results in larger amounts of simulated low clouds due to insufficient representation of fine-scale eddies acting across sharp thermodynamic gradients atop the mixed layer (Khairoutdinov et al., 2009; Muller & Held, 2012; Pauluis & Garner, 2006; Yanase et al., 2020).

Few studies have specifically investigated the sensitivity of convective aggregation to *vertical* resolution. However, given the sensitivity of simulated clouds to vertical resolution, it is reasonable to expect convective aggregation to behave differently at different vertical grid spacings. High clouds are particularly sensitive to model vertical resolution (Gu et al., 2011; Ohno & Satoh, 2018; Ohno et al., 2019; Seiki et al., 2015). Changes in high cloud coverage with vertical resolution may have a strong effect on atmospheric radiative cooling. This, in turn, can impact upgradient circulations driven by low clouds in dry columns. Consequently, convective aggregation may also be influenced. Vertical resolution also impacts the simulation of low clouds, with finer vertical grid spacing better able to reproduce both the observed mid-tropospheric cloud top mode associated with temperature inversions near the freezing level (Inness et al., 2001; Khairoutdinov et al., 2009; Retsch et al., 2017; Roeckner et al., 2006) and boundary layer clouds, which are sensitive to the simulated thermodynamic structure and turbulence of the layer (Bretherton et al., 1999; Guo et al., 2008; Marchand & Ackerman, 2010; Stevens et al., 2003, 2005). Therefore, one way vertical resolution may impact convective aggregation is through its influence on simulated low cloud amount.

The rate at which cloudy, humid air mixes with relatively dry, cloud-free air directly influences cloud buoyancy (Holloway & Neelin, 2009; Kuang & Bretherton, 2006; Molinari et al., 2012; Romps & Kuang, 2010; Singh & O'Gorman, 2013, 2015; Zipser, 2003), the distribution of cloud top heights (e.g., Carpenter et al., 1998; Derbyshire et al., 2004), the humidity of the cloud-free environment (Romps, 2014; Singh et al., 2019), and the thermal stratification of the tropical upper troposphere (Singh & O'Gorman, 2013; Singh & O'Gorman, 2015). Mixing also impacts convective aggregation. Tompkins and Semie (2017) argue that strong mixing rates, which more readily dilute and suppress the vertical growth of clouds in dry regions, are necessary for convective aggregation in simulations. Becker et al. (2017) emphasize the key role of mixing by entrainment in the sensitivity of convective aggregation to sea surface temperature. At higher temperatures, mixing of dry, environmental air into updrafts reduces updraft buoyancy more than at colder temperatures, thereby encouraging convection to aggregate more readily.

Grid resolution serves as a control on mixing rates in simulations. In global CRM simulations with the Nonhydrostatic ICosahedral Atmospheric Model (NICAM), Ohno et al. (2019) demonstrate a strong dependence of turbulent mixing rates on vertical resolution. They found significantly stronger turbulent diffusivity at coarse vertical resolution (38 levels), resulting in nearly double the global high cloud fraction (21.5%) compared to identical simulations with high vertical resolution (13.5% for 398 levels). This sensitivity was attributed to the dependence of turbulent diffusivity in their sub-grid scale (SGS) mixing parameterization on local vertical grid spacing. Parishani et al. (2017) show that refining the vertical mesh of CRMs embedded in a superparameterized climate model led to increases in boundary layer vertical velocity variance. Mixing rates also depend on simulation grid spacing independent of numerical sensitivities of SGS mixing parameterizations on resolution. Jeevanjee and Zhou (2022) show a similar dependence of high cloud fraction to *horizontal* resolution in simulations with the Finite-Volume Cubed-Sphere Dynamical Core (FV³), where no SGS mixing scheme is employed. They find the highest high cloud fraction in simulations with the finest horizontal grid spacing, hypothesizing that this results from more efficient mixing at high horizontal resolution, leading to more evaporation of condensed water in the free-troposphere. Consequently, larger updraft mass fluxes produce the same amount of net latent heating needed to balance radiative cooling (which they hold constant in their simulations). Given the dependence of mixing rates on resolution, and the dependence of simulated convective aggregation on mixing rates, another way that vertical resolution may impact convective aggregation is via a control on turbulent mixing.

Vertical resolution may also impact convective aggregation through its influence on simulated cold pools, the intensity and dissipation of which are sensitive to grid resolution (Bryan & Morrison, 2012; Grant & van den Heever, 2016). Previous studies also emphasize the importance of spatially varying surface fluxes for convective aggregation (Bretherton et al., 2005; Muller & Held, 2012; Wing & Emanuel, 2014). Observational studies
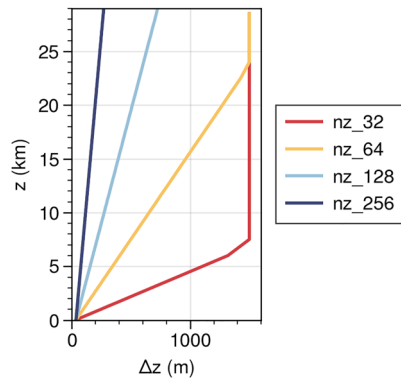
Figure 1. Grid spacing, Δz, of the vertical grids used in SAM simulations.

demonstrate that surface fluxes are also sensitive to convective aggregation (Tobin et al., 2012). Therefore, to the extent that vertical resolution influences surface fluxes, feedbacks involving surface fluxes may be involved in determining the sensitivity of convective aggregation to vertical resolution.

Vertical resolution is often an overlooked free parameter in simulations of deep convection, especially of convective aggregation. In this study, we investigate the impact of vertical resolution on the simulated behavior of deep convection, with a focus on convective aggregation. We demonstrate that vertical resolution directly affects simulated profiles of clouds, temperature, and humidity across spatial scales, as well as influences the occurrence, onset time, and equilibrium intensity of aggregated convection.

2. Methods

2.1. Simulations

We use the System for Atmospheric Modeling (SAM, version 6.10.9) in this study, described in Khairoutdinov and Randall (2003). SAM is a non-hydrostatic anelastic model with doubly-periodic boundary conditions, which conserves liquid water static energy. We use the original SAM1MOM single-moment microphysics scheme (Khairoutdinov & Randall, 2003), the original SGS turbulence scheme (Khairoutdinov & Randall, 2003) which predicts SGS turbulent kinetic energy (TKE) using a 1.5-order closure, and the Rapid Radiative Transfer Model for GCM Applications (RRTMG; Clough et al., 2005; Mlawer et al., 1997). The model employs Newtonian damping in the top third of the model to prevent gravity wave reflection. Simulations are run in non-rotating radiative-convective equilibrium with perpetual solar insolation set to 551.58 W m^{-2} at a zenith angle of 42.05° (equivalent to the annual mean over 20°S–20°N) as in Wing et al. (2018), carbon dioxide concentrations at 355 ppm, and a stratospheric ozone layer. We use an ocean surface with a constant sea surface temperature of 300 K, and initiate convection by adding white noise to the initial surface air temperature field. The time step, which is permitted to halve up to a limit of 40 times, is set to a maximum of 5 s.

We use four different vertical grids (Figure 1) with 32, 64, 128, and 256 vertical levels, which each linearly ramp from a grid spacing of about 45 m (lowest two model levels) to a maximum of 1,500 m, up to a model top with a rigid lid at 30 km. This approach of linearly ramping vertical grids is commonplace in experiments using CRMs (e.g., Bryan & Morrison, 2012; Muller & Held, 2012; Tompkins & Craig, 1998; Wing et al., 2018; Yanase et al., 2020). We use the naming convention "nz_X" where X represents the number of vertical levels in each model run. For instance, "nz_32" indicates the coarsest vertical resolution. We chose this vertical resolution design to ensure that the vertical grid spacing is fine enough in the lower troposphere to reliably resolve the boundary layer inversion and strong lower tropospheric water vapor gradient in all simulations. As a result, nz_32's vertical grid reaches the maximum grid spacing of 1,500 m around 7.5 km, while the finest resolution grid, nz_256, has vertical grid spacing less than 50 m throughout the troposphere.

We run three sets of simulations: a small domain, a medium domain, and a large domain. We choose the domain sizes to loosely follow the Radiative-Convective Equilibrium Model Intercomparison P (RCEMIP) protocol (Wing et al., 2018). The small domain is square, with 128 points in the horizontal directions and a horizontal grid spacing of 1 km (domain size of 128 km × 128 km). The medium domain is rectangular, with 128 × 384 points in each horizontal direction, respectively, and a horizontal grid spacing of 3 km (domain size of 384 km × 1,152 km). Both the small and medium domain simulations were initialized with the same warm, moist tropical thermodynamic profile (access the initial sounding at Jenney, 2023). Medium domain simulations were initialized using different white noise initial conditions (see Section 3.2).

Convective self aggregation occurs in large domains (always in square domains larger than 500 km) with relatively coarse grid spacing (always when grid spacing exceeds 2 km) (Muller & Held, 2012; Yanase et al., 2020). In our simulations, the large domain is also square, with 512 points in the horizontal directions and a horizontal grid spacing of 3 km (domain size of 1,536 × 1,536 km). We use a square instead of the long channel shape employed in RCEMIP in order to run the simulations using more parallel tasks and speed up compute time. Following Wing et al. (2018), the large domain simulations were initialized from equilibrated small domain

soundings, using the domain averaged temperature and humidity profile from each vertical resolution for the last 10 days of each simulation. Large domain simulations also have stronger solar insolation at 650.83 W m^{-2} and a zenith angle of 50.5° (annual mean incident radiation over 5–10°N). This difference is a result of updating the insolation values during manuscript preparation and revisions, excluding the large domain simulation due to computational limitations.

Simulations are run for 140 (small domain) and 150 (medium and large domain) days. Three-dimensional instantaneous variables (i.e., "snapshots") were saved four times per day for small and medium domain simulations, and once every 12 hr for large domain simulations. Two-dimensional column integrated or surface level statistics, which represent averages across all model time steps, were saved more frequently. We do not run medium or large domain simulations at the highest vertical resolution (nz_256) due to the high computational expense.

2.2. Diagnostics

In our analysis of convective aggregation, we use a mass-weighted vertical integral of frozen moist static energy, $\langle h_f \rangle$, the spatial variance of which is a commonly used metric for convective aggregation (e.g., Becker et al., 2017; Holloway & Woolnough, 2016; Huang & Wu, 2022; Matsugishi & Satoh, 2022; Patrizio & Randall, 2019; Wing & Emanuel, 2014):

$$\langle h_f \rangle = \frac{1}{g} \int_{p_{top}}^{p_{bottom}} (c_p T + gz + L_v q_v - L_f q_i) dp. \tag{1}$$

In Equation 1, g is the gravitational acceleration, p is pressure (with subscripts referencing values at model top and bottom), c_p is the specific heat capacity of dry air at constant pressure, T is air temperature, z is altitude, L_v and L_f are the latent heats of vaporization and fusion, respectively, and q_v and q_i are the mixing ratios of water vapor and condensed ice (cloud plus precipitating), respectively.

We investigate physical mechanisms that influence tendencies of the spatial variance of $\langle h_f \rangle$ as in many previous studies (e.g., Arnold & Putman, 2018; Becker et al., 2017; Beydoun & Hoose, 2019; Carstens & Wing, 2022; Chen & Wu, 2019; Coppin & Bony, 2015; Holloway & Woolnough, 2016; Huang & Wu, 2022; Matsugishi & Satoh, 2022; Patrizio & Randall, 2019; Wing & Cronin, 2016; Wing & Emanuel, 2014). The budget equation for $\langle h_f \rangle$ is

$$\frac{\partial \langle h_f \rangle}{\partial t} = LW + SW + SEF - \nabla_h \cdot \langle h_f \vec{\mathbf{u}} \rangle, \tag{2}$$

where LW and SW are the net atmospheric vertical convergences of longwave and shortwave radiation, respectively, SEF is the surface latent plus sensible heat flux into the atmosphere, and $-\nabla_h \cdot \langle h_f \vec{\mathbf{u}} \rangle$ is the vertically-integrated horizontal flux convergence of h_f (henceforth, the "moisture flux convergence," MFC). Following Wing and Emanuel (2014), we horizontally linearize Equation 2 and multiply by $\langle h_f \rangle'$ to obtain the budget equation for the spatial variance of $\langle h_f \rangle$:

$$\frac{1}{2} \frac{\partial \langle h_f \rangle'^2}{\partial t} = \langle h_f \rangle' \left[LW' + SW' + SEF' - \nabla_h \cdot \langle h_f \vec{\mathbf{u}} \rangle' \right], \tag{3}$$

where primes represent deviations from the horizontal domain-mean. We calculate each term except the last term on the right hand side using daily means of simulation output, and then calculate the last term as a residual from this budget, as was done in Bretherton et al. (2005), Muller and Held (2012), and Wing and Emanuel (2014).

Finally, we summarize the spatial organization of the large domain simulations during various periods by reorganizing the 2D horizontal space into 100-element, 1D column relative humidity percentiles, and conditioning state variables therein. We define column relative humidity as the mass-weighted vertically-integrated water vapor (precipitable water) divided by the precipitable water of the same column at water vapor saturation. Following Bretherton et al. (2005) and Schulz and Stevens (2018), we calculate the mass streamfunction, Ψ, in column relative humidity percentile space as

$$\Psi_i(z) = \Psi_{i-1}(z) + \bar{\rho}(z) w_i(z) \alpha, \tag{4}$$
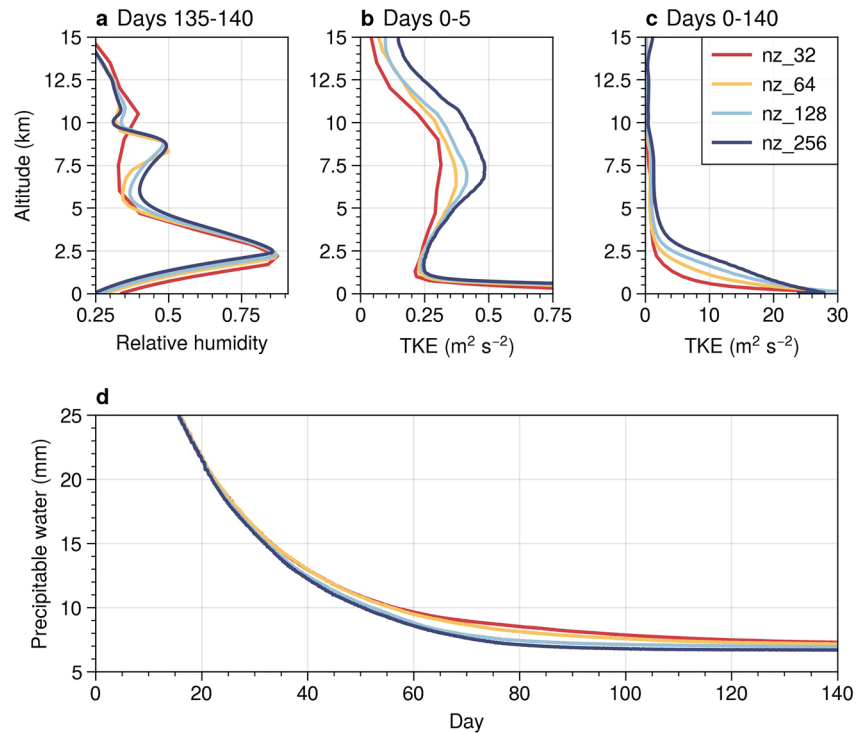
Figure 2. For small domain simulations with no sub-grid scale parameterization or surface fluxes, domain- and time-mean profiles of (a) relative humidity averaged over days 135–140, (b) turbulent kinetic energy (TKE) averaged over days 0–5 (c) TKE averaged over days 0–140; (c) domain-mean precipitable water.

where i is an index referencing the column relative humidity percentile bin, $\bar{\rho}$ is the mean density profile, w is the vertical velocity binned by column relative humidity percentile, and α is a weight given by 1 divided by the number of bins. Ψ is calculated by starting at the driest bin and assuming $\Psi = 0$ there. This method yields closed streamfunction contours because the simulations conserve mass and have no net circulation.

3. Results

3.1. Small Domain Simulations

First, we assess the impact of vertical resolution on convective aggregation in simulations with a small domain size (128 km × 128 km).

3.1.1. No-SGS Parameterization

In a global CRM, Ohno et al. (2019) show that coarse vertical resolution simulations produce the same high cloud cover as high resolution simulations when the turbulent length scale within the SGS turbulence parameterization is set to the high resolution value. Inspired by this finding, we begin by presenting our simplest case: a set of small domain simulations with no SGS parameterization, and without any surface fluxes ("no-SGS"). Our objective is to examine the sensitivity of the evolution of the humidity field to vertical resolution in the absence of SGS physics and surface moisture input into the atmosphere.

Figure 2 displays selected statistics from these simulations. As both surface and lateral sources of water vapor are zero, column water vapor continuously lowers from its initialized value as condensed water precipitates out (Figure 2d). Despite similar final values of precipitable water (range of 0.6 mm between the highest and lowest resolutions), vertical resolution impacts final vertical distributions of water vapor throughout the lower troposphere (Figure 2a). The high resolution cases are less humid below 2.5 km and more humid in the overlying troposphere (from about 2.5 to 10 km). This difference is due to enhanced mixing from higher resolved turbulence at high resolution (Figures 2b and 2c), which lifts water vapor from the moist lower levels upwards, where it can condense and precipitate out. Consequently, nz_256 experiences a faster decrease in precipitable water. The key
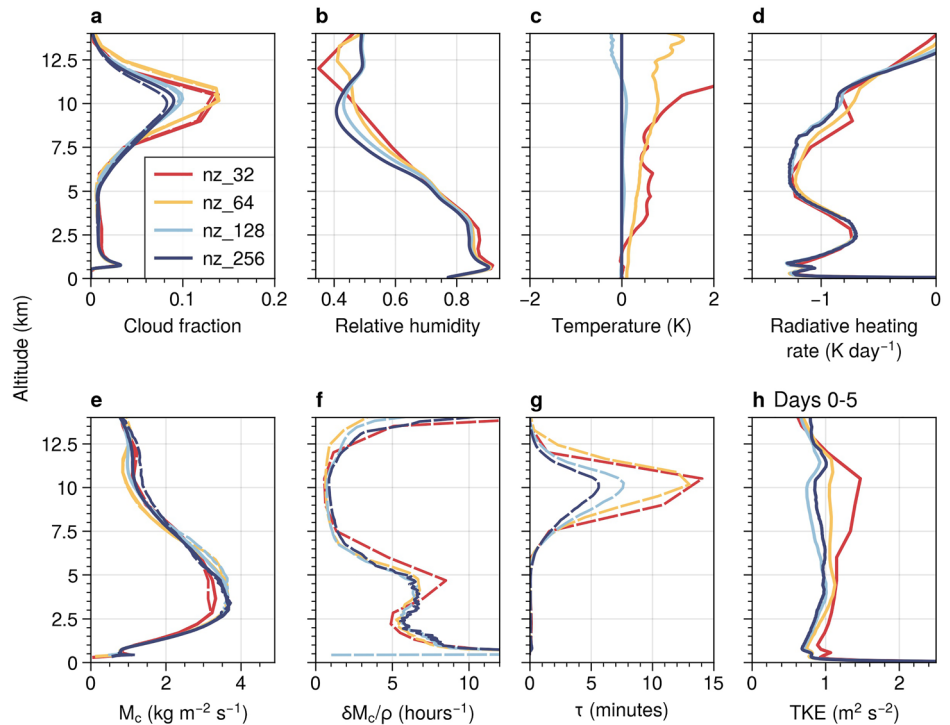
Figure 3. For small domain simulations with a sub-grid scale parameterization and interactive surface fluxes, time- and horizontal-mean profiles of (a) Cloud fraction, (b) relative humidity, (c) temperature difference from nz_256, (d) net radiative heating rate, (e) updraft mass flux, (f) volumetric detrainment rate, (g) cloud lifetime, (h) turbulent kinetic energy (TKE) from days 0–5. Dashed lines represent profiles calculated using 10-day extensions. All other profiles are for days 40–140.

result here (which will later help inform conclusions from subsequent, less idealized simulations) is that higher free-tropospheric relative humidity at high vertical resolution is a direct result of enhanced resolved turbulence.

3.1.2. With SGS Parameterization

Next, we shift our focus to small domain simulations *with* a SGS parameterization and interactive surface fluxes. Our objective here is to assess the degree to which vertical resolution affects specific processes in a simulation with more physical realism, while excluding large-scale convective organization, which otherwise tends to dominate statistics of radiative-convective equilibrium (e.g., Becker et al., 2017).

Figure 3 shows time- and horizontally-averaged profiles for the simulations. Consistent with Ohno et al. (2019), high cloud fraction is sensitive to vertical resolution, especially above 7 km. The coarsest resolutions produce the highest cloud fractions, with cloud fraction generally decreasing with increasing vertical resolution (although high cloud fraction above 10 km is larger for nz_64 than nz_32). We define cloud fraction at each time and model level as the fraction of grid cells with cloud condensate mixing ratios above 10^{-3} g kg^{-1}. Also consistent with previous studies, relative humidity is sensitive to vertical resolution (Figure 3b), with the most humid mean profile in the lowest resolution case, and the driest in the highest resolution case (Roeckner et al., 2006; Tompkins & Emanuel, 2000); note this is the opposite humidity response than we found in the simulations of Section 3.1.1 that excluded SGS effects. Figure 3c shows the mean temperature profile difference from nz_256. The mean temperature is roughly the same between the nz_128 and nz_256 cases, with the nz_32 and nz_64 cases being warmer, especially above 10 km. This aligns with other studies (Lee et al., 2019; Roeckner et al., 2006; Tompkins & Emanuel, 2000) that report colder upper tropospheres when using higher vertical resolution. Figure 3d illustrates that radiation profiles are quite similar below 6 km, but show some variation with vertical resolution between 6 and 10 km, with the magnitude of radiative cooling larger for nz_128 and nz_256 than for nz_32 and nz_64.

Figure 4 shows the time evolution of various fields in the small domain simulations, showing that the overall spread in system behavior is controlled by changes in high cloud and relative humidity leading to downstream effects on
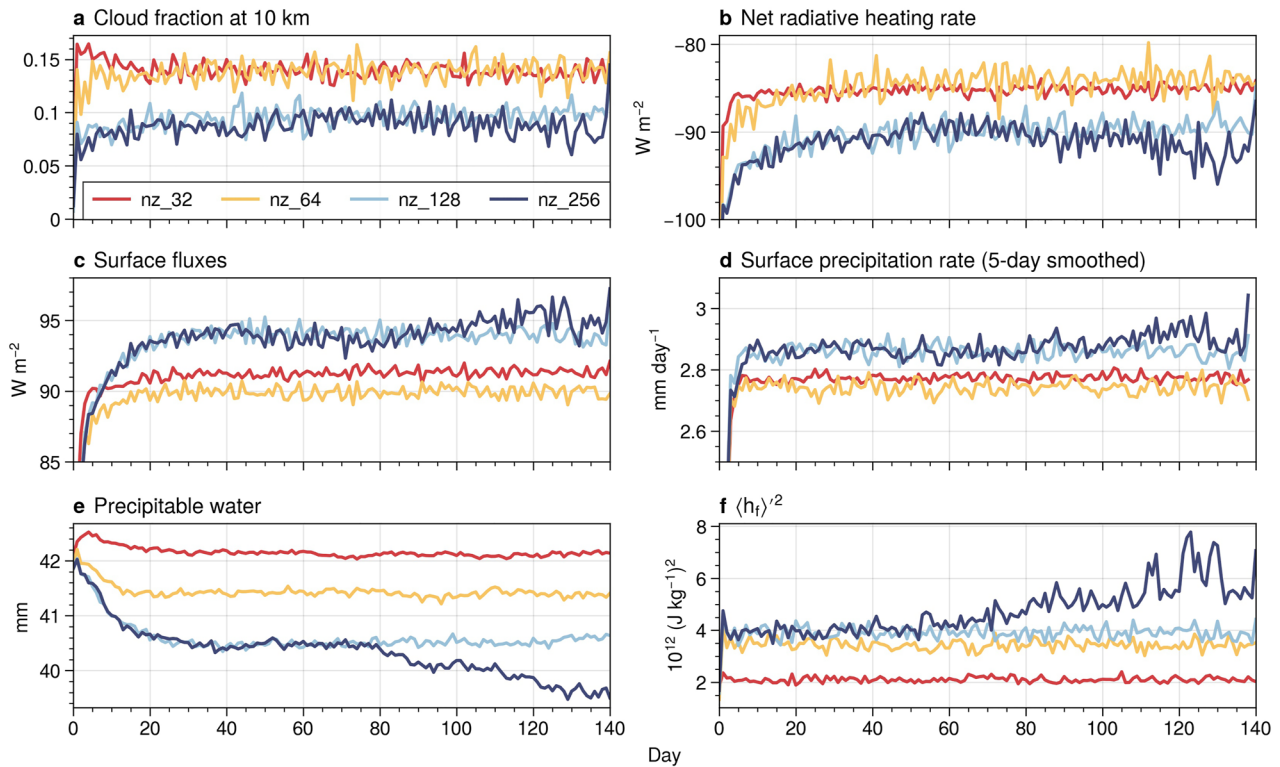
Figure 4. For small domain simulations, daily-mean (a) cloud fraction at 10 km, (b) net atmospheric radiative heating rate, (c) surface fluxes (sensible plus latent), (d) surface precipitation rate (with a centered running-mean window of 5 days applied for smoothing), (e) precipitable water, and (f) $\langle h_f \rangle'^2$.

precipitation and surface fluxes through a radiative feedback. The spread in high cloud fraction (Figure 4a) and the net atmospheric radiative heating rate (Figure 4b), calculated as the difference between the net radiative flux at the surface and the net radiative flux at the top of the atmosphere, are both established immediately, reaching equilibrium after 20 days. For both fields, the resolutions group into two modes: the coarser resolutions (nz_32 and nz_64) display larger high cloud fractions and less radiative cooling than the higher resolutions (nz_128 and nz_256), which cool more due to their lower ice cloud coverage and lower free-tropospheric relative humidities (the combination of which leads to high transmissivity of radiation emitted from low levels). Surface fluxes and precipitation also adjust quickly, with higher values for nz_128 and nz_256 needed to balance the additional atmospheric longwave cooling (Figures 4c and 4d). The change in column water vapor with resolution is opposite to that of precipitation, implying that precipitation is more efficient at high vertical resolution. Finally, the spatial variance of $\langle h_f \rangle$, $\langle h_f \rangle'^2$, increases with vertical resolution (Figure 4f), implying a wider column water vapor distribution at high vertical resolution. Interestingly, all of the simulations experience a steady state equilibrium except for nz_256, which begins a transition around days 60–70. We return to this later.

We now investigate the mechanisms underlying the spread in both high cloud fraction and relative humidity.

3.1.2.1. Control of High Cloud by Relative Humidity Via Sublimation

Beydoun et al. (2021) show that the equilibrium high cloud fraction, A, is well captured by the approximation

$$A \approx \frac{\delta M_c}{\rho}\tau, \qquad (5)$$

where δ is the fractional detrainment rate, M_c is the updraft mass flux, ρ is the air density, and τ is the high cloud lifetime. We estimate the volumetric detrainment rate, $\delta M_c/\rho$, using the cloud water plus ice (henceforth, "cloud water") budget as in Seeley et al. (2019), from 10-day simulation extensions where spatially resolved cloud water microphysics tendencies are saved:
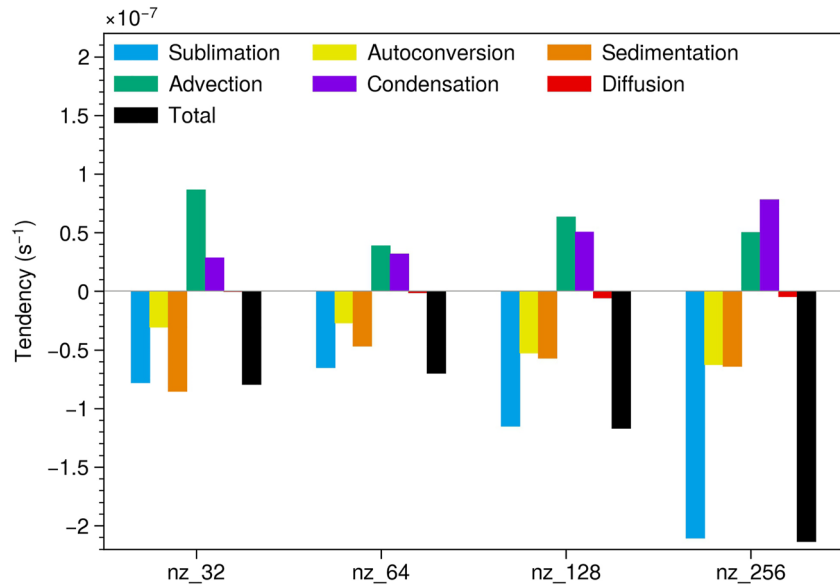
$$\delta M_c q_{c0} = e + p_c, \qquad (6)$$

Figure 5. For 10-day extensions of small domain simulations, the mean tendency of cloud water at 10 km due to various processes and its total, taken over cloudy grid cells.

where q_{c0} is the mean cloud condensate mixing ratio of updraft air, e is the mean cloudy non-updraft cloud water evaporation and sublimation rate, and p_c is the mean cloudy non-updraft rate of cloud water conversion to precipitating water. We define cloudy grid cells and updrafts roughly following Seeley et al. (2019), where "cloudy" grid cells are those with cloud water mixing ratios greater than 10^{-5} kg kg^{-1}. Updrafts are cloudy grid cells with vertical velocities exceeding a height-varying threshold (10^{-5} m s^{-1} below 500 m, which linearly increases to 1 m s^{-1} at 3 km, above which it stays constant at 1 m s^{-1}). Resulting profiles of M_c, $\delta M_c/\rho$, and τ from Equations 5 and 6 are shown in Figures 3e–3g.

Above 7 km, there is almost no spread in the volumetric detrainment rate, $\delta M_c/\rho$ (Figure 3f). Spread in high cloud fraction with vertical resolution is instead driven by spread in high cloud lifetime, τ, which decreases with increasing vertical resolution (Figure 3g). High cloud lifetime is the inverse of the total cloud water tendency over cloudy grid cells (Beydoun et al., 2021). Figure 5 shows these mean tendencies at 10 km. As implied by decreasing τ with increasing resolution, the total negative cloud water tendency (black bars) increases in magnitude (i.e., becomes more negative) with vertical resolution. This increase is driven by a large increase in cloud water sublimation with vertical resolution. While changes in other terms with resolution occur, they are mostly offset by changes of equal magnitude but opposite sign in another term; autoconversion nearly balances condensation, and sedimentation nearly balances advection. Diffusion is a relatively small term.

So far we have implicated a sensitivity of high cloud sublimation to vertical resolution as a key control on high cloud amount, but this can be viewed as a consequence of a more fundamental humidity control. In SAM's single moment microphysics scheme, cloud evaporation and sublimation occurs via saturation adjustment, which prevents supersaturation and allows cloud water/ice to exist only in a saturated environment. As a result, increased cloud sublimation at 10 km at high resolution can be attributed to the lower relative humidity at that altitude.

3.1.2.2. Turbulent Kinetic Energy as a Driver

What drives the spread in relative humidity in the upper troposphere (between 6 and 11 km) with vertical resolution? The mean profile of resolved TKE (we omit SGS TKE, which is about 2 orders of magnitude smaller than the resolved component) during the first five days of the simulations (Figure 3h) hints at a probable origin rooted in turbulent mixing due to resolved turbulence. In the previous section, we showed that in simulations with no SGS scheme, enhanced resolved turbulence at high vertical resolution led to more mixing of water vapor out of the boundary layer and higher tropospheric relative humidities. In contrast, in simulations with SAM's SGS scheme enabled, mean profiles of relative humidity and TKE both exhibit a decrease with vertical resolution, and the largest spread in the same layer (between 6 and 10 km). This decrease is driven by a decrease in resolved TKE

in cloud-free grid cells, rather than in convective regions (Figure S1 in Supporting Information S1). This suggests that the spread in relative humidity in SAM is driven by resolved turbulent transport in cloud-free regions, which is affected by the SGS scheme used for these simulations. The absence of any SGS scheme results in larger resolved TKE with increased resolution (Section 3.1.1). The aim of an SGS scheme is to quantify the "missing" (unresolved) energy at sub-grid scales (which is larger for coarser grids), and its interactions with resolved scales. Ideally, and all else equal, the sum of the resolved and SGS turbulence should be invariant with resolution. Here, we have shown that for SAM's SGS turbulence scheme, this is not the case.

Putting it together, we pose that the causality leading to the small domain sensitivities to vertical grid spacing summarized in Figures 3 and 4 is as follows. Increasing vertical resolution causes:

- Less total TKE via the SGS component's sensitivity to grid resolution, which is strong enough to overwhelm the increase in resolved TKE, leading to
- Less upper tropospheric humidity due to less ventilation of boundary layer air aloft, in turn causing
- More high cloud evaporation and reduced high cloud lifetimes, leading to
- Less high cloud amounts, and thus
- More radiative cooling, surface fluxes and precipitation.

Finally, we return to the departure of nz_256 from steady-state behavior, which begins around day 80 (Figure 4). At that time, domain-mean precipitable water decreases while $\langle h_f \rangle'^2$ increases, indicating the growth of dry regions as convection becomes more organized. This suggests that nz_256 is starting to aggregate (Held et al., 1993). Visual inspection of precipitable water snapshots at day 140 confirm the horizontal expansion and further drying of dry regions (Figure S2 in Supporting Information S1), although convection has not yet fully aggregated into one connected region.

The onset of convective aggregation in a small domain (approximately 100 km) with a horizontal resolution of 1 km is surprising. Typically, for horizontal resolutions less than 2 km, aggregation of convection requires domain sizes of about 500 km (Muller & Held, 2012; Yanase et al., 2020). This is because cold pool circulations transport moisture into the dry regions surrounding convection, which can homogenize boundary layer moisture when the domain is small (Jeevanjee & Romps, 2013; Yanase et al., 2020). Our results suggest that in nz_256, there is (at least) one physical mechanism that increases moist static energy in humid columns, and/or removes moist static energy from dry columns, that is strong enough to combat downgradient moistening from cold pools. We suspect that increased spatial variance in atmospheric radiative heating, specifically stronger longwave cooling and reduced shortwave absorption (enabled by the presence of dry columns uncontaminated by high cloud coverage from nearby convection), plays a role. By enhancing radiative cooling in already dry regions, radiation may then further reduce the moist static energy of dry columns, thereby increasing the spatial variance of moist static energy, promoting organization.

3.2. Medium Domain Simulations

Next, we assess the impact of vertical resolution on convective aggregation in simulations with a medium domain size (384 km × 1,152 km).

Medium domain simulations are run with a horizontal resolution and domain size that are both large enough to facilitate convective aggregation, according to the aggregation versus no aggregation regime boundaries found in Muller and Held (2012) and Yanase et al. (2020). However, as we will soon demonstrate, convection only aggregates in nz_64 (we did not run a nz_256 case with a medium domain size).

The initial effects of vertical resolution match our expectations from the small domain runs. Figures 6a–6e shows profiles of cloud fraction, relative humidity, temperature, radiative heating rate, and updraft mass flux for the first 10 days of the simulations before aggregation occurs. As in the small domain simulations, cloud fraction and relative humidity decrease with increasing resolution. Differences in temperature, radiative heating, and updraft mass flux are relatively small in the first 10 days of the simulations.

On longer timescales, where we expect clouds to aggregate in all of our medium domain simulations, we find a previously unreported sensitivity to vertical resolution. Figures 7a–7f illustrates snapshots of precipitable water from simulation days 5 and 150. On day 5, all cases are disaggregated, with a relatively homogeneous distribution of precipitable water. Similar to the small domain simulations, domain-mean values of precipitable water
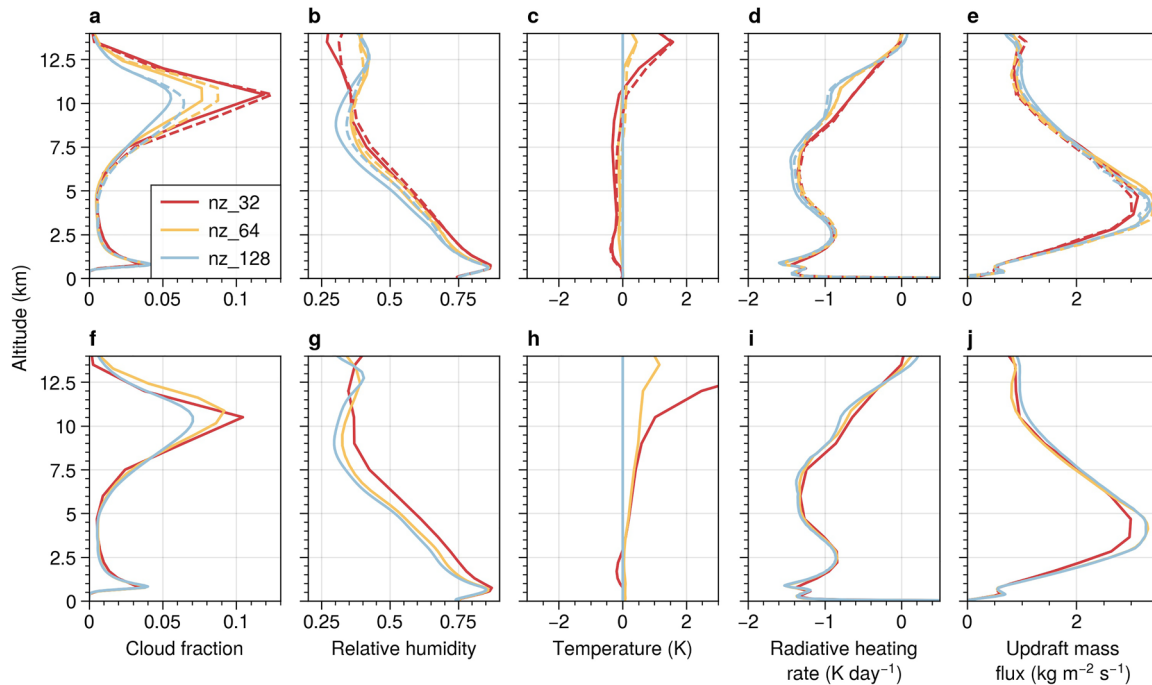
Figure 6. For days 0–10 of the medium (top row) and large (bottom row) domain simulations, profiles of (a, f) cloud fraction, (b, g) relative humidity, (c, h) temperature deviation from nz_128, (d, i), radiative heating rate, and (e, j) updraft mass flux. Dashed and solid lines indicate the two different initial conditions.

decrease while the spatial variance increases with increasing resolution (see also Figure 10b). By day 150, aggregation is clearly evident in nz_64. This occurs as dry, subsiding patches of air gradually expand, confining deep convection to a singular region. The large, dry region that emerges by day 150 in nz_64 is much drier than any region in the disaggregated state at day 5.

We confirm the robustness of the finding that only nz_64 supports aggregation at this domain size with an additional set of medium domain simulations run with a different random white noise initialization. Figures 8a and 8c show daily-mean values of the mid-tropospheric subsidence fraction and $\langle h_f \rangle'^2$, both commonly-used metrics for quantifying and marking the onset of convective aggregation (e.g., Coppin & Bony, 2015; Wing et al., 2020). Larger values of each metric indicate a higher degree of convection aggregation. Figures 8a and 8c demonstrate that for both sets of medium domain simulations, nz_64 aggregates while the other vertical resolutions do not. Aggregation onset and equilibrium (i.e., the time at which $\langle h_f \rangle'^2$ stops increasing) occur around the same time for both nz_64 runs, around days 10, and 60, respectively (Figure 8c).

We find that adiabatic terms are chiefly responsible for this sensitivity, by examining the $\langle h_f \rangle'^2$ budget (see Equation 3 and Section 2.2). Figure 9 shows the time series of each term in the budget for the first 20 days of the medium domain simulations, alongside accumulated tendencies in time. During the first 10 days, for all resolutions, both longwave radiation and surface fluxes positively contribute to the total $\langle h_f \rangle'^2$ tendency, with the largest contributions from longwave heating. This is expected (e.g., Bretherton et al., 2005; Muller & Held, 2012). In general, the MFC term negatively contributes to the total tendency, while the shortwave term is negligible. In nz_64, shortly before day 10, the total tendency begins increasing, indicating the onset of convective aggregation. The magnitudes of the accumulated tendency for all terms are similar across resolutions, except for the MFC term, which is slightly smaller for nz_64. Therefore, for nz_64, the instability that triggers aggregation is enabled not by stronger diabatic feedbacks with spatial $\langle h_f \rangle$ anomalies, but instead by relatively weaker horizontal homogenization of $\langle h_f \rangle$ by the circulation. Once aggregation begins in nz_64, rapid increases in the shortwave term contributes to further aggregation.

The horizontal MFC term plays a crucial role in determining aggregation behavior across different resolutions (i.e., encouraging it in nz_64 and suppressing it for the other resolutions). The terms on the right side the $\langle h_f \rangle'^2$ budget represent covariances between local anomalies of vertically-integrated physical process rates
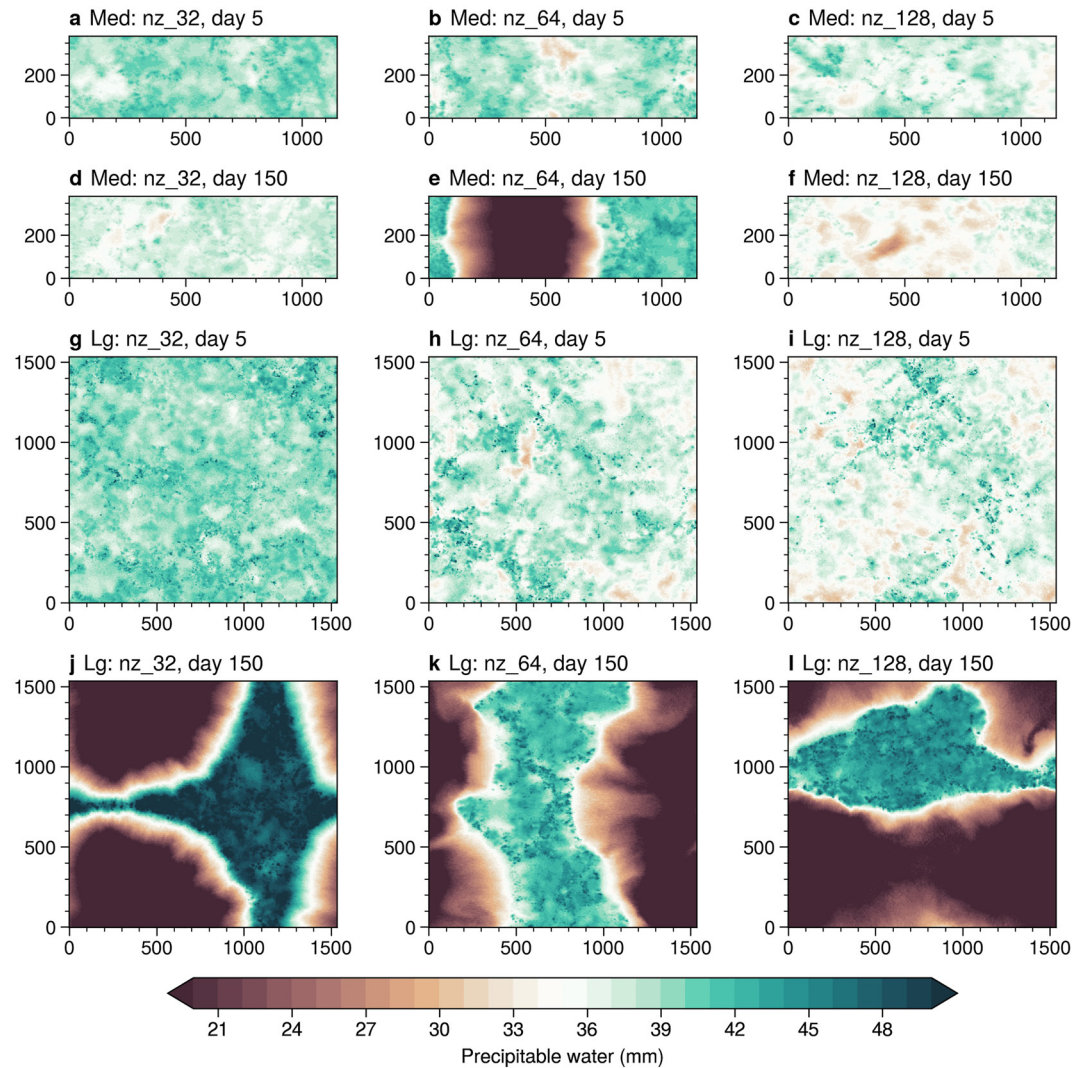
Figure 7. For the medium ("Med"; top two rows) and large ("Lg"; bottom two rows) domain simulations, snapshots of precipitable water on days 5 and 150. Note that only one set of the medium domain simulations is shown.

(e.g., atmospheric longwave heating) and local $\langle h_f \rangle$ anomalies. The magnitude of this term is influenced by the magnitude of $\langle h_f \rangle'^2$, the spatial variance of MFC, and the correlation between local $\langle h_f \rangle$ anomalies with local MFC anomalies. Figure 10 shows the correlation between and the respective standard deviations of $\langle h_f \rangle$ and MFC anomalies for the first 10 days. For reference, the aggregation of nz_64 was assisted by a small MFC term. Figure 10 shows that this is primarily driven by weaker correlations between local $\langle h_f \rangle$ and local MFC anomalies (panel a), rather than weaker standard deviations of $\langle h_f \rangle$ or MFC (panels b and c).

What prevents aggregation in the nz_32 and nz_128 simulations? For nz_32, despite a smaller standard deviation of $\langle h_f \rangle$ (Figure 10b) and MFC (Figure 10c), adiabatic resistance to aggregation is strengthened due to stronger correlations with $\langle h_f \rangle$ anomalies. Evidently, coarse vertical resolution changed the spatial organization of moisture reorganization by the circulation relative to convective anomalies. The inhibition pathway for nz_128 is different. The large MFC term is due to larger spatial variances in both $\langle h_f \rangle$ and MFC, which overwhelm intermediate values of correlations between the two. Thus, in addition to widening the humidity distribution (via the increase of dry columns), increasing vertical resolution also led to stronger anomalies of moisture homogenization by the circulation, both of which strengthened adiabatic resistance to convective organization. This strong MFC term for nz_128 appears to prevent aggregation, despite having slightly larger magnitudes of the longwave and surface flux terms in the first 7 days, and a resultant higher accumulated total tendency compared to nz_64 during that time.
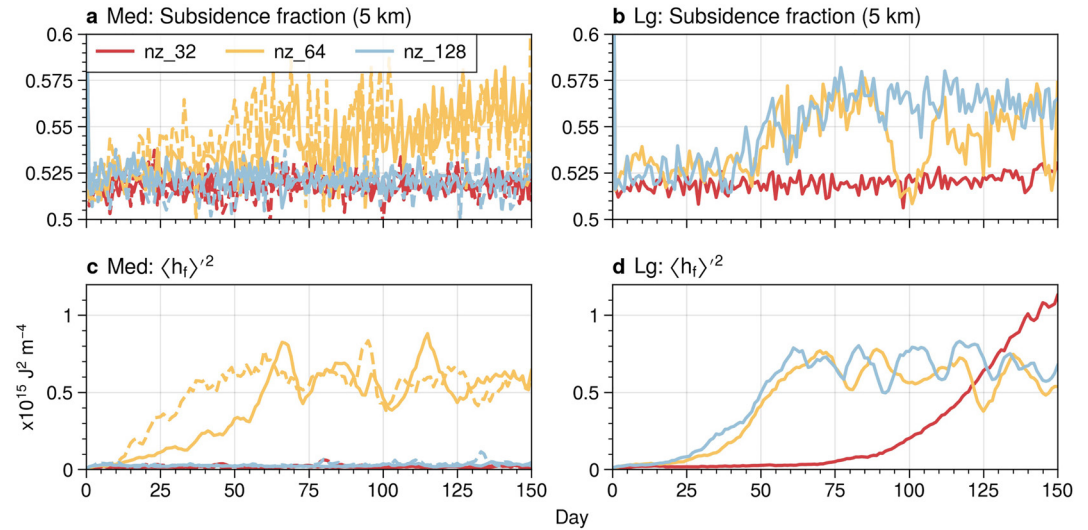
Figure 8. For the medium ("Med"; left column) and large ("Lg"; right column) domain simulations, the daily-mean (a, b) 5 km subsidence fraction, and (c, d) $\langle h_f \rangle'^2$. Dashed and solid lines indicate the two different initial conditions.

In summary, our analysis of medium domain simulations has highlighted that there remains unexplored numerical sensitivity on the conditions for aggregation that may have been missing in past studies, revealed by considering variations in the vertical grid: Two out of three simulations that we expected to aggregate did not, through separate pathways that both acted to enhance adiabatic resistance to the onset of organization.

For further reference, we include selected mean profiles from days 50–150 in Supporting Information S1 (Figure S3 in Supporting Information S1).

3.3. Large Domain Simulations

Lastly, we assess the impact of vertical resolution on convective aggregation in simulations with a large domain (1,536 km × 1,536 km).

Figures 6f–6j shows profiles of cloud fraction, relative humidity, temperature, radiative heating rate, and updraft mass flux for the first 10 days of the simulations before aggregation occurs. As in the small and medium domain simulations, cloud fraction and relative humidity decrease with increasing resolution. Differences in temperature, radiative heating, and updraft mass flux are relatively small in the first 10 days of the simulations.

Unlike the small and medium domain simulations, convection in the large domain simulations aggregates for *all* resolutions. Figures 7g–7l illustrates snapshots of precipitable water from simulation days 5 and 150. On day 5, all cases are disaggregated, and precipitable water is relatively homogeneous. Similar to the small and medium domain simulations, higher resolutions result in a drier domain and wider spatial distribution of precipitable water. By day 150, convection has clearly aggregated: the distribution of precipitable water has widened considerably, and organized into one cohesive moist region and one cohesive very dry region.

Figures 8b and 8d show the mid-tropospheric (5 km) subsidence fraction and $\langle h_f \rangle'^2$ for the large domain simulations. These show that aggregation occurs around the same time for nz_64 and nz_128, with onset beginning around day 20 and reaching equilibrium around day 60. After day 60, convection remains aggregated for both cases and exhibits oscillating behavior around some equilibrium point, as in Patrizio and Randall (2019). The behavior of nz_32 is considerably different. Aggregation occurs later, with an onset period starting around day 70 that lasts longer than that of nz_64 and nz_128. By day 150, nz_32 has not reached equilibrium, and exhibits a value of $\langle h_f \rangle'^2$ that is approaching twice as large as the equilibrium values of the other cases. Despite nz_32 having not yet reached an aggregated equilibrium value of $\langle h_f \rangle'^2$, it is beginning to show oscillating behavior, which, for the other cases, occurs at equilibrium rather than during aggregation onset (Figure 8d). This suggests that nz_32 may be near equilibrium by day 150.
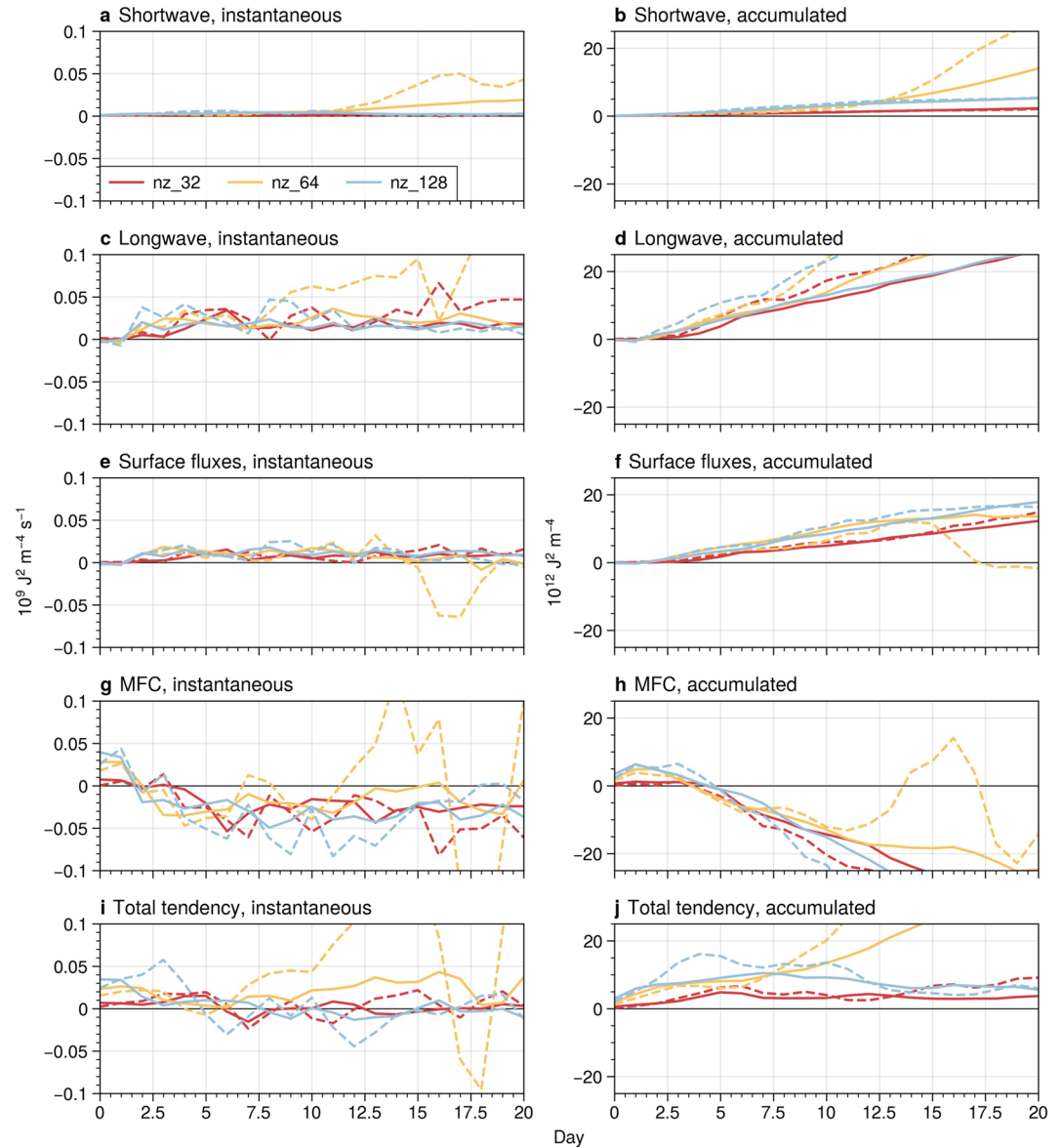
Figure 9. For the first 20 days of the medium domain simulations, time series of instantaneous (left column) and temporally-integrated from simulation day 0 (right column) tendencies of each term in the budget equation for the spatial variance of $\langle h_f \rangle$ anomalies (Equation 3). Dashed and solid lines indicate the two different initial conditions.

Next, we use the $\langle h_f \rangle'^2$ budget (see Equation 3 and Section 2.2) to investigate physical mechanisms responsible for simulated differences in aggregation between the nz_32 and the other cases. We first focus on the period marking the early onset of aggregation for nz_64 and nz_128, and no aggregation for nz_32. Figure 11 shows the time series of each term in the budget for the first 25 days of the large domain simulations, alongside accumulated tendencies in time. Across all vertical resolutions, shortwave heating, longwave heating, and surface flux anomalies all positively covary with $\langle h_f \rangle$ anomalies, and hence positively contribute to the total $\langle h_f \rangle'^2$ tendency. Horizontal circulations (i.e., the MFC term) negatively contribute to the total tendency. During this period, for nz_64 and nz_128, the accumulated total tendency continuously increases and the spatial distribution of $\langle h_f \rangle$ becomes more organized (Figure 11j), indicating the onset of aggregation. For nz_32, the total tendency remains at a near-constant value, indicating that aggregation is not occurring.

Consistent with previous studies, the initiation of convective aggregation for both nz_64 and nz_128 is associated with positive horizontal covariances in longwave and surface flux anomalies with $\langle h_f \rangle$ anomalies (e.g.,
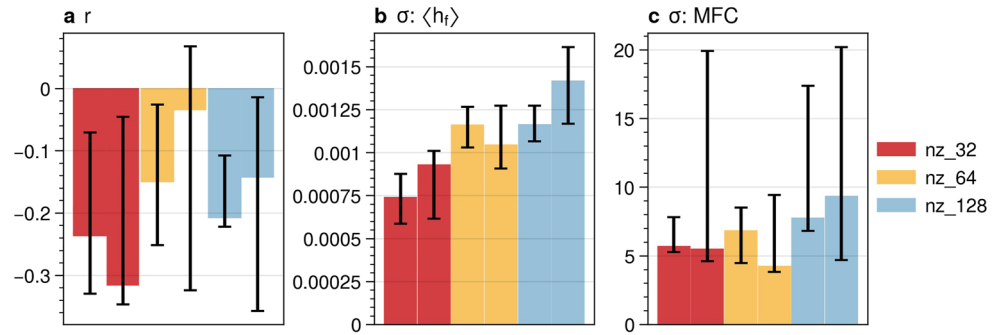
Figure 10. For the first 10 days of the medium domain simulations, daily median values of (a) the correlation coefficient between $\langle h_f \rangle$ anomalies and MFC anomalies, (b, c) the normalized spatial standard deviations of $\langle h_f \rangle$ and MFC anomalies, respectively. Error bars enclose the 25th to 75th percentile of daily values.

Bretherton et al., 2005; Muller & Held, 2012). Shortly before aggregation, the shortwave term also starts to increase, although its contribution to the total tendency is much smaller. Aggregation occurs in nz_64 and nz_128 because, taken together, the diabatic processes that increase $\langle h_f \rangle'^2$ are increasing $\langle h_f \rangle'^2$ faster than horizontal circulations can homogenize it. In contrast, during this early period for nz_32, positive contributions to the total tendency are balanced by the negative contribution from the MFC term, meaning that aggregation does not occur.

The magnitudes of each term in the $\langle h_f \rangle'^2$ budget are smaller in nz_32 than in the higher resolution cases. This difference is more clearly visualized in the accumulated tendency (right) column of Figure 11. The lower magnitudes of the nz_32 tendency terms are driven by one or a combination of three factors: smaller $\langle h_f \rangle'^2$, smaller spatial variances in the process rates, and/or smaller magnitude correlations of local $\langle h_f \rangle$ anomalies with process anomalies. Figure 12 shows the spatial correlation coefficient and normalized standard deviation for terms in the $\langle h_f \rangle'^2$ budget for the first 10 days of the large domain simulations. The local daily correlations between $\langle h_f \rangle$ anomalies and process rates have larger magnitudes for nz_64 and nz_128 than for nz_32. Additionally, as we saw in medium-domain simulations, the spatial standard deviation of $\langle h_f \rangle$ is also larger for nz_64 and nz_128. The standard deviations of longwave and shortwave anomalies are comparable between cases. Both surface fluxes and MFC have larger standard deviations for nz_64 and nz_128. This indicates that the larger magnitudes of the budget terms for nz_64 and nz_128 are driven by larger correlations between local processes and $\langle h_f \rangle$ anomalies, as well as a wider spatial distribution of $\langle h_f \rangle$. Furthermore, the surface fluxes and MFC terms also have an additional contribution from increased spatial variance in their respective process rates.

To gain a better understanding of why the correlations between $\langle h_f \rangle$ with radiative and MFC are larger at higher resolutions, we visualize how clouds, radiation, and the overturning circulation are organized in moisture space during the early period of each simulation (see Section 2.2). Figure 13 shows the radiative cooling rate, mass streamfunction, Ψ (see Equation 4), cloud condensate mixing ratio, and h_f binned by column relative humidity percentile for simulation days 0–25. The spatial organization of these fields is generally similar between cases. However, as in the small domain simulations, there is larger high cloud coverage at low vertical resolution (the white contours between 7 and 12 km in Figures 13a–13c extend further into dry columns at coarse resolution than at high resolution; see Figure S4 in Supporting Information S1 for differences between nz_32 and higher resolutions for the same period). Low clouds exhibit opposite behavior, with cloud coverage at 1 km extending further into the dry region at high resolution. In the wettest columns (above 95th percentile), clouds at 1 km have much larger condensed water mixing ratios at nz_64 and nz_128, resulting in stronger radiative heating in those regions (see Figure S4 in Supporting Information S1). This seems to be driving the larger correlations of radiative heating anomalies with $\langle h_f \rangle$ seen in Figure 12a. We also note stronger radiative cooling just above the boundary layer in nz_64 and nz_128 throughout the domain, although the correlation with $\langle h_f \rangle$ is negative rather than positive (i.e., stronger radiative cooling in moist columns). In the rest of the domain, differences in radiative heating between nz_32 and the higher resolution cases are small.

Generally, Ψ has a similar shape and magnitude across all cases. However, there is enhanced mid-level horizontal motion from dry to wet columns between 2 and 4 km, as well as enhanced low-level inflow (below 2 km) into moist columns in nz_64 and nz_128. These features may contribute to the stronger negative correlations in Figure 12a.
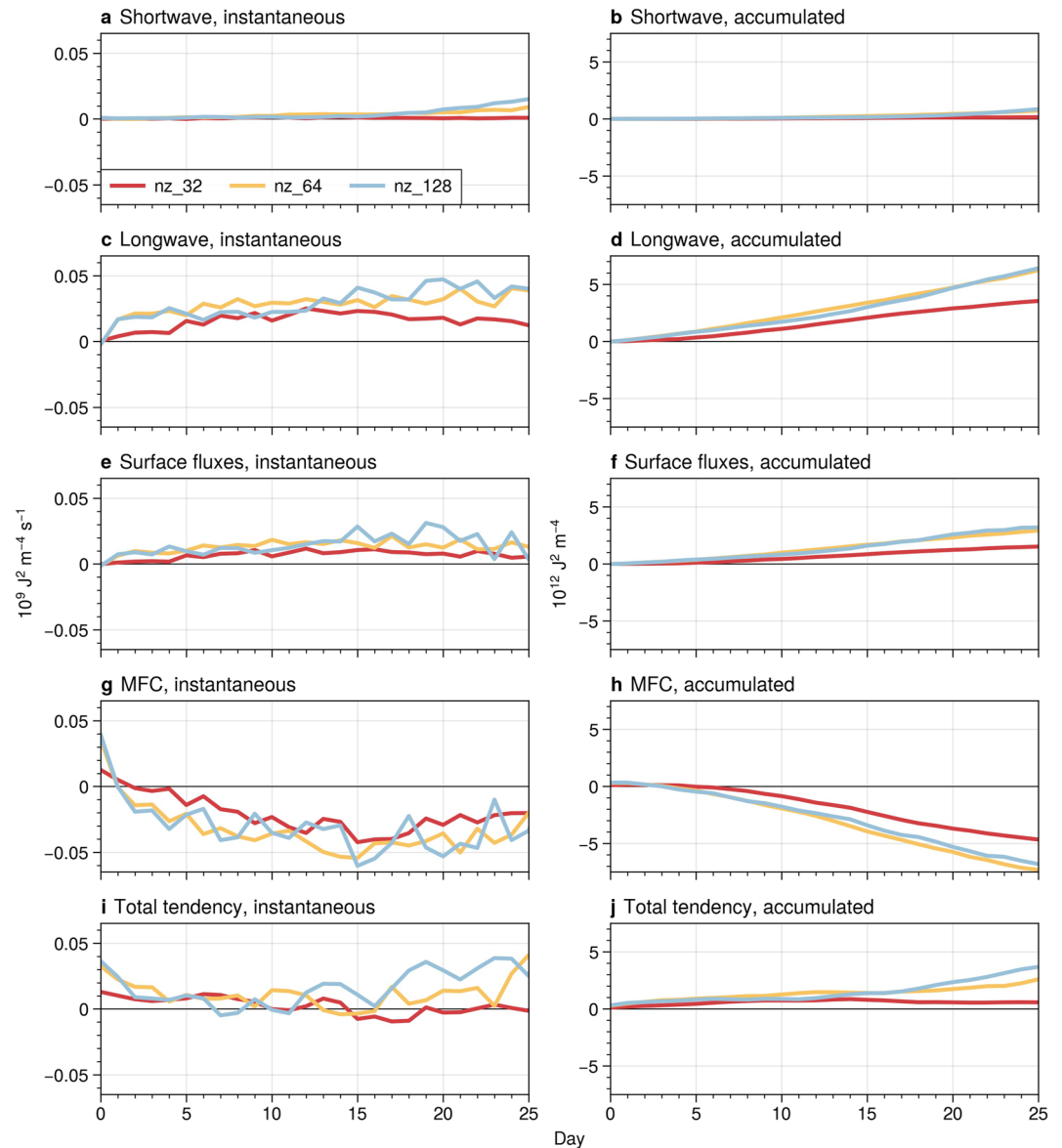
Figure 11. For the first 25 days of the large domain simulations, time series of instantaneous (left column) and temporally-integrated from simulation day 0 (right column) tendencies of each term in the budget equation for the spatial variance of $\langle h_f \rangle$ anomalies (Equation 3).

To conclude our analysis of the early period, we seek to understand the larger standard deviations of surface fluxes and MFC in nz_64 and nz_128. Figure 14 shows distributions of wind speed, water vapor mixing ratio, and water vapor mixing ratio saturation depression for simulation days 2–10 for the lowest model level. The surface wind speed distribution systematically widens with resolution. Distributions of both the water vapor mixing ratio and saturation depression exhibit an increasingly drier tail at high resolution. Taken together, the wider distribution of wind speeds and more frequent occurrence of low humidities at higher resolution explain the wider surface flux distribution. This is because large values of the latent heat flux are possible at high wind speeds and high saturation depression. The widening distribution of surface wind speeds and water vapor mixing ratio may also contribute to the increasing standard deviation of the MFC with increasing resolution.

Although nz_32 does not aggregate during the early period, aggregation onset begins by day 70. Figure 15a shows the $\langle h_f \rangle'^2$ budget for the full simulation period for nz_32 (alongside nz_64 and nz_128 for reference). Unlike aggregation in the higher resolution cases, growth of the total $\langle h_f \rangle'^2$ tendency in nz_32 is due to a positive
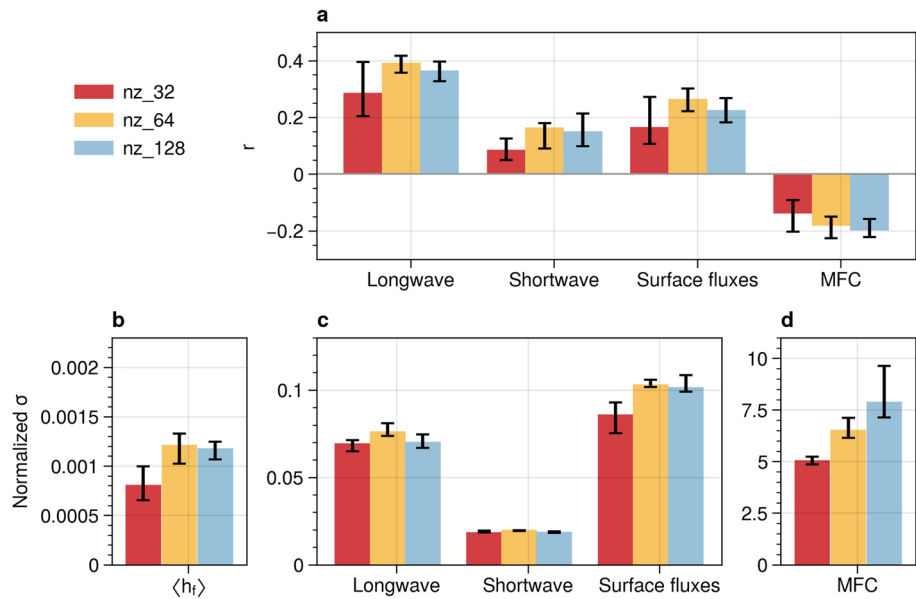
Figure 12. For first 10 days of the large domain simulations, median daily values of (a) the correlation coefficient between local process rate anomalies and $\langle h_f \rangle$ anomalies, and (b–d) normalized spatial standard deviations of variables in the $\langle h_f \rangle$ budget (Equation 2). Error bars in all panels show 25th to 75th percentile of daily values.
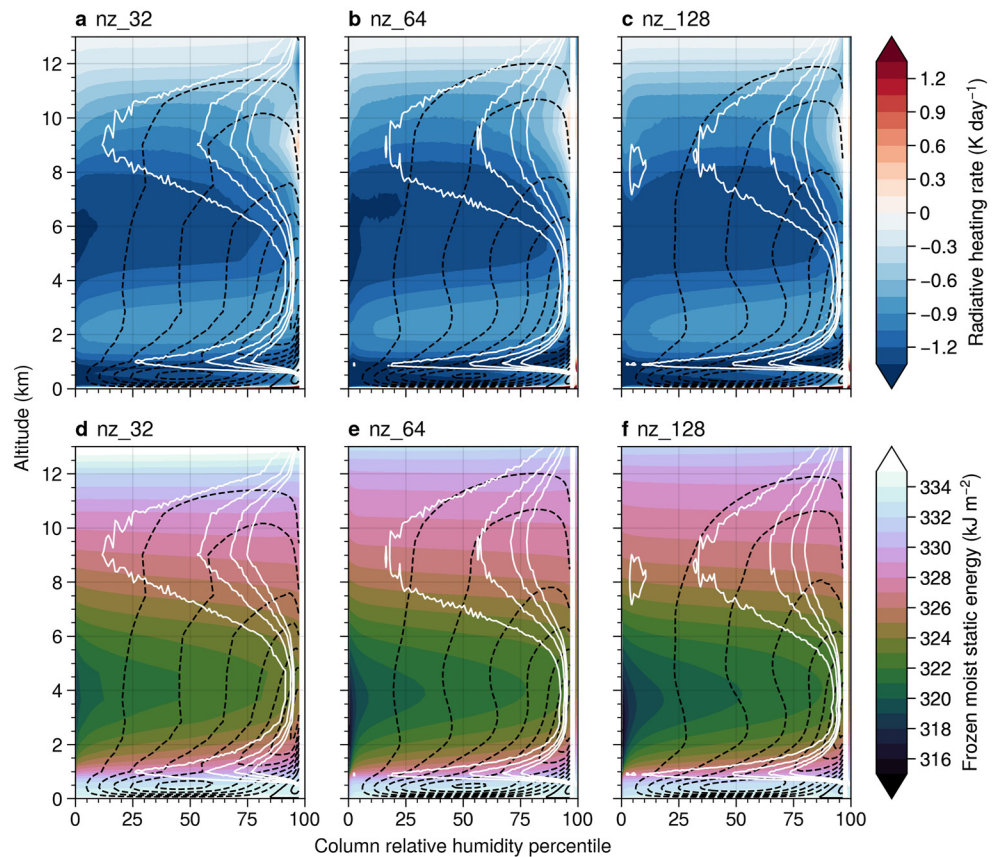

Figure 13. For the first 25 days of the large domain simulations, (a–c) radiative heating rate (filled contours), cloud condensate mixing ratio (white contours drawn at 0.003, 0.006, 0.009, 0.012 g kg^{-1}), and mass streamfunction (black contours drawn every 1 g m^{-2} s^{-1}), each binned by column relative humidity percentile; (d–f) as in top row but filled contours show h_f.
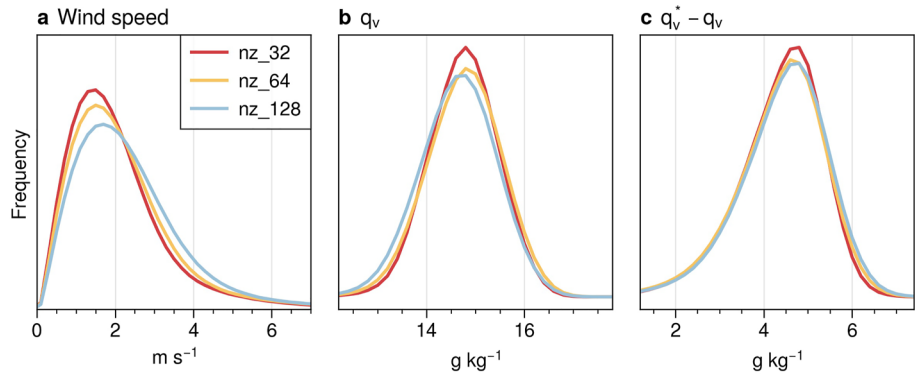
Figure 14. For days 2–10 of the large domain simulations, lowest model level distributions of (a) wind speed, (b) water vapor mixing ratio, and (c) water vapor saturation depression (saturation mixing ratio minus observed mixing ratio).

fluctuation of the MFC term superimposed on a very slowly growing shortwave term (which began increasing around day 45, not shown). Beyond that point, further aggregation is primarily controlled by the MFC term, with smaller contributions from the shortwave term, and to an even smaller degree, the longwave term. This differs
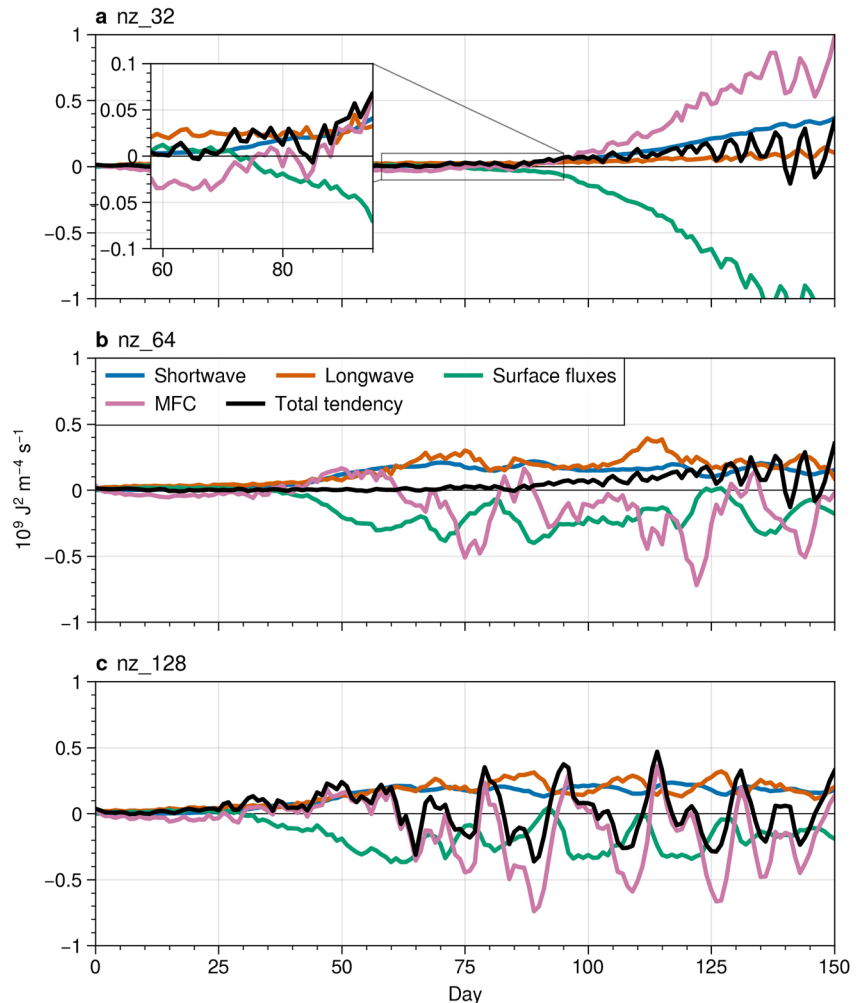

Figure 15. For large domain simulations, time series of instantaneous tendencies of each term in the budget equation for the spatial variance of $\langle h_f \rangle$ anomalies (Equation 3).
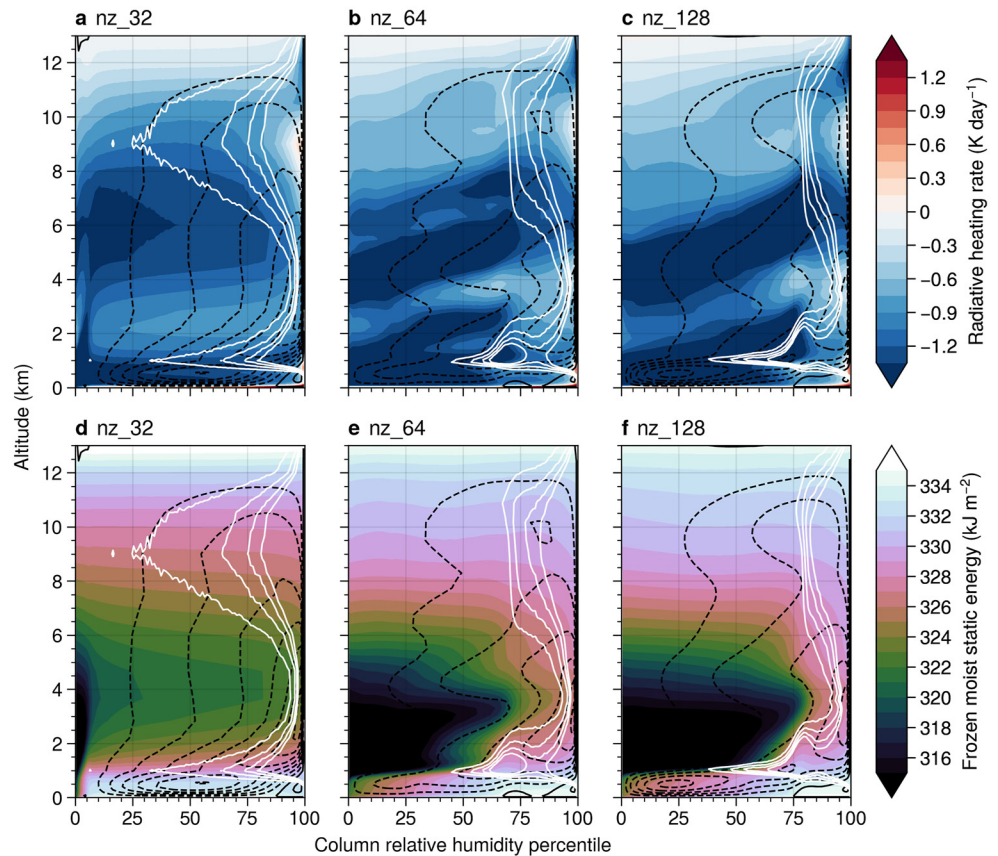
Figure 16. For large domain simulation days 75–100, (a–c) radiative heating rate (filled contours), cloud condensate mixing ratio (white contours drawn at 0.003, 0.006, 0.009, and 0.012 g kg^{-1}), and mass streamfunction (black contours drawn every 1 g m^{-2} s^{-1}), each binned by column relative humidity percentile; (d–f) as in top row but filled contours show h_f.

from the onset of aggregation in nz_64 and nz_128, where contributions from shortwave, longwave, and MFC terms are of equal magnitude.

Figure 16 shows quantities binned by column relative humidity for simulation days 75–100, which marks the early growth period of aggregation for nz_32, and mature stages of aggregation for nz_64 and nz_128. For nz_32, high cloud fraction in dry columns has diminished, enabling slightly stronger radiative cooling in those columns. The structure of the effective overturning circulation remains largely unchanged from the early period. However, the most notable difference between nz_32 during this period compared to early period, as well as between it and the other cases, is the structure of h_f, which shows *very* low values that extend down to the surface. In contrast, h_f remains relatively high below 1 km for previous times and in the other cases (despite the mature aggregation of nz_64 and nz_128 at this time). The emergence of these very dry columns indicates that growth of the shortwave term in the $\langle h_f \rangle'^2$ budget is driven by reduced shortwave absorption in progressively drying columns.

The exceptional dryness of the boundary layer in the driest columns of nz_32 is a unique feature of this resolution. The very large reduction in boundary layer h_f explains why $\langle h_f \rangle'^2$ is able to surpass that of nz_64 and nz_128 (Figure 8d). Boundary layer h_f is heavily weighted in $\langle h_f \rangle$. Furthermore, the extreme relative minimum in boundary layer h_f in nz_32's dry columns also explains why MFC and surface fluxes eventually reach relatively large magnitudes (Figure 15a) beyond day 105. Low-level mass divergence out of the dry region (e.g., due to subsidence) can efficiently export moist static energy to more humid columns because of the very strong gradient in boundary layer moist static energy. Conversely, surface fluxes in the dry region can very efficiently moisten those columns (a negative feedback with $\langle h_f \rangle'^2$) because of the extreme dry boundary layer.

What, then, permits extreme boundary layer drying in nz_32, but not in nz_64 and nz_128? One possibility may be the strength of cold pools, which help homogenize boundary layer moisture (Jeevanjee & Romps, 2013; Yanase et al., 2020). Figure S5 in Supporting Information S1 shows that large negative virtual temperature anomalies,

(relatively dense air, i.e., stronger cold pools) occur less frequently in nz_32 compared to nz_64 and nz_128. The causes of the exceptional boundary layer drying in nz_32 warrant further investigation, which we leave for future work.

To conclude our analysis of the large domain simulations, we comment on the equilibrated spatial organization of moisture, radiation, and the circulation in nz_64 and nz_128 (Figures 16b, 16c, 16e, and 16f). Consistent with Sokol and Hartmann (2022), there is an intensification of the mid-tropospheric congestus circulation with aggregation in nz_64 and nz_128. This feature is largely absent in nz_32, possibly due to the fact that at this time, aggregation is still underway. It is also possible that coarse vertical resolution may also play a role (Inness et al., 2001; Retsch et al., 2017; Roeckner et al., 2006). Above 1 km, maxima in radiative cooling of nz_64 and nz_128 follow horizontal motion indicated by the streamfunction contours. This is consistent with the horizontal motion being associated with detrainment of clouds and moisture, with strong radiative cooling occurring at the tops of clouds and moist layers. At this time, the horizontal extent of low clouds has decreased, pulling toward more humid columns, especially in the higher resolution cases where aggregation is most mature. Meanwhile, the vertical extent and thickness of low clouds has grown for columns between the 50th and 85th percentiles, with both features exhibiting greater enhancement in nz_128. Lastly, high cloud coverage in both nz_64 and nz_128 is reduced, consistent with the decrease in the area coverage of humid ascending air that accompanies aggregation (Figures 7 and 8).

For further reference, we include selected mean profiles from days 50–150 in Supporting Information S1 (Figure S3 in Supporting Information S1).

4. Discussion and Conclusions

We investigate the impact of vertical resolution on small (128 km × 128 km), medium (384 km × 1,152 km) and large (1,536 km × 1,536 km) domain simulations of explicit convection in radiative-convective equilibrium using the System for Atmospheric Modeling (SAM) CRM. We use vertical grids with 32, 64, 128, and 256 levels (although we do not run medium or large domain simulations with 256 levels because of the high computational expense).

Results from the small domain simulations reveal that high vertical resolution produces cooler upper troposperes, lower relative humidity, and reduced high cloud coverage. The reduction in high cloud coverage is a consequence of shorter cloud lifetimes, driven by enhanced evaporation due to the lower humidity. We suspect that spread in relative humidity with vertical resolution in SAM arises from disproportionate turbulence damping by the SGS parameterization, leading to enhanced turbulence at low vertical resolution. These findings are in agreement with the results of Ohno et al. (2019), who also found reduced high cloud coverage at high resolution in a different CRM due to a numerical sensitivity of the turbulent mixing length to vertical resolution. The combination of a drier free troposphere and reduced high cloud coverage at high vertical resolution results in enhanced atmospheric radiative cooling, surface fluxes, and precipitation. Increases in precipitation with vertical resolution occur despite simultaneous decreases in precipitable water, and larger values of the gross evaporation-to-condensation ratio that occurs throughout most of the troposphere.

Novel results of our study emerge from our analysis of the sensitivity of convective self aggregation to vertical resolution.

Muller and Held (2012) and Yanase et al. (2020) find roughly the same boundary separating the occurrence and non-occurrence of convective aggregation based on domain size and horizontal resolution. Despite our small domain simulations having a domain size and horizontal resolution well within the *non*-aggregation regime defined by these studies, our highest resolution case began to show signs of aggregation.

On the other hand, the medium domain simulations, which have a domain size and horizontal resolution well within the aggregation regime of Muller and Held (2012) and Yanase et al. (2020), only aggregated in the simulations with 64 vertical levels. Yanase et al. (2020) discuss that the domain size required for aggregation is set by competition between near-surface circulations: one driven by dry region radiative cooling (which exports moisture from the dry region), and the other driven by evaporative cooling of falling rain (which imports moisture to the dry region). Horizontal resolution plays a role in this competition, with coarser resolution enhancing dry region radiative cooling due to the thickening of low clouds, thereby reducing the domain size needed for

aggregation. Our study confirms that the strength of horizontal moisture homogenization by circulations is an important determinant in whether aggregation occurs in simulations with varying vertical resolutions. For the first time, however, our findings suggest that vertical resolution also influences horizontal moisture circulations, and impacts the domain size at which aggregation occurs. We note that Muller and Held (2012) and Yanase et al. (2020) used vertical grids with 64 levels.

Wing et al. (2018) propose that convective aggregation may be less sensitive to numerical details in domains with rectangular geometries. Here, we have shown sensitivity of convection aggregation to vertical resolution in domains with rectangular domains. Our results suggest that the aspect ratio at which convective aggregation becomes insensitive to numerics may be much larger than the 3-to-1 aspect ratio used in our medium domain simulations.

Unlike the small and medium domain simulations, convection aggregated in all of the large domain cases. Generally, nz_64 and nz_128 behaved similarly, displaying similar onset times, growth mechanisms, equilibrium characteristics, and spatial organization of aggregation. In contrast, nz_32 behaved uniquely, showing delayed onset, and different onset and growth mechanisms.

During the early period of the large domain simulation, nz_32 does not aggregate. This can be attributed, in part, to its low spatial variance in column humidity, surface fluxes, and moisture convergence. These are likely related to stronger mixing, lower near-surface wind speeds, and a narrower and moister distribution of near-surface relative humidity. Additionally, we find weaker correlations of column moist static energy anomalies and anomalies in radiative heating, surface fluxes, and MFC.

Eventually, nz_32 begins to aggregate in the latter half of the simulation, starting around day 70. This appears to be facilitated by a slow but extreme drying of the boundary layer in its driest columns, which leads to a reversal in moisture reorganization by the circulation, triggering aggregation. Interestingly, the intensity of aggregation (quantified as $\langle h_f'\rangle^2$) eventually exceeds that of nz_64 and nz_128 by nearly twofold. Weak cold pools may play a role in this process, but confirmation of this is left for future work.

Cloud dilution suppresses the vertical growth of clouds in dry regions and thus promotes convective aggregation (Becker et al., 2017; Tompkins & Semie, 2017). Due to enhanced mixing at coarse vertical resolution, one may expect aggregation to occur more readily in nz_32 compared to the higher vertical resolution cases. Estimates of the bulk fractional entrainment from the small domain simulations, which use the difference in moist static energy between updrafts and the environment, are nearly resolution invariant (not shown). This suggests that updraft dilution is similarly resolution-invariant. This occurs because of the decreasing difference between updraft and environmental humidity, despite decreasing turbulence at high resolution. This means that although turbulent mixing between updrafts and the environment may be stronger at coarse resolution, convective plumes are not more diluted because the entrained air is more humid. This may help explain why nz_32 does not aggregate despite stronger mixing.

We note that the large domain simulations were initialized with equilibrated profiles of temperature and humidity from the small domain simulations, which differed with resolution. It is possible that some of the simulated differences in convective aggregation were impacted by these differences in the initial profiles. However, the medium domain simulations, which were initialized with the same moist tropical thermodynamic profile, also exhibit robust sensitivities to vertical resolution.

We speculate whether the convective aggregation behavior of a medium or large domain simulation with 256 vertical levels would differ significantly from nz_64 and nz_128. In the small domain simulations, nz_128 and nz_256 behaved somewhat similarly in the early stages of the simulation: both exhibited similar mean profiles of cloud fraction and temperature, as well as similar time evolution of atmospheric radiative heating, surface fluxes, surface precipitation, and precipitable water. However, the nz_256 simulation began to display signs of convective aggregation around day 80 and had a drier mean profile and increased evaporation of condensed water. For instance, would aggregation have also been suppressed in the medium domain simulations as it was for nz_128? This remains to be seen.

Understanding the sensitivity of deep convection to model formulation is essential for interpreting and applying simulations of deep convection for physical understanding and decision-making. For example, our results suggest that the vertical resolution of CRMs embedded in multi-scale climate models (through a process referred to as

"superparameterization" or "multi-scale modeling framework," in which CRMs *replace* the convective parameterization) can impact the simulated mean global cloud and relative humidity fields, subsequently affecting the global radiative budget. Therefore, the vertical resolution of embedded CRMs may be a tunable parameter. CRMs are also commonly used to *inform* convective parameterizations, and there is a growing movement to utilize CRM simulations to create data-driven (i.e., machine learning-derived) convective parameterizations. The variability of simulated deep convection with vertical resolution shown here, including the magnitudes of certain physical processes (e.g., cold pool and mean radiative intensity), emphasizes the need to constrain convective parameterizations with observations. Furthermore, CRMs with limited domains are one tool actively used to study tropical high clouds and their response to warming (e.g., Mackie & Byrne, 2023). Our study finds that in at least one CRM (SAM), high cloud fraction is sensitive to vertical resolution. It remains to be seen whether the high cloud response to warming is similarly sensitive in SAM as it is in other CRMs (Ohno et al., 2019).

In summary, we have demonstrated that vertical resolution has significant impacts on simulations of deep convection, including convective aggregation. Vertical resolution directly impacts simulated profiles of clouds, temperature, and humidity, and affects the onset time and equilibrium intensity of aggregated convection. Additionally, vertical resolution appears to affect the domain size at which convective aggregation can occur. We suspect that the sensitivity to vertical resolution in SAM is driven by disproportionate turbulence damping by the SGS parameterization, which leads to enhanced turbulence and domain-mean relative humidity at low vertical resolution. These findings emphasize the need to improve the representation of mixing processes in atmospheric simulations.

Data Availability Statement

Convection resolving model simulations were conducted with the System for Atmospheric Modeling (SAM) version 6.10.9 (Khairoutdinov, 2022). SAM model configuration files (vertical grids and initial soundings) are hosted on GitHub (Jenney, 2023).

References

Arnold, N. P., & Putman, W. M. (2018). Nonrotating convective Self-Aggregation in a limited area AGCM. *Journal of Advances in Modeling Earth Systems*, *10*(4), 1029–1046. https://doi.org/10.1002/2017ms001218

Becker, T., Stevens, B., & Hohenegger, C. (2017). Imprint of the convective parameterization and sea-surface temperature on large-scale convective self-aggregation. *Journal of Advances in Modeling Earth Systems*, *9*(2), 1488–1505. https://doi.org/10.1002/2016ms000865

Beydoun, H., Caldwell, P. M., Hannah, W. M., & Donahue, A. S. (2021). Dissecting anvil cloud response to sea surface warming. *Geophysical Research Letters*, *48*(15), e2021GL094049. https://doi.org/10.1029/2021gl094049

Beydoun, H., & Hoose, C. (2019). Aerosol-cloud-precipitation interactions in the context of convective self-aggregation. *Journal of Advances in Modeling Earth Systems*, *11*(4), 1066–1087. https://doi.org/10.1029/2018ms001523

Bretherton, C. S., Blossey, P. N., & Khairoutdinov, M. (2005). An Energy-Balance analysis of deep convective Self-Aggregation above uniform SST. *Journal of the Atmospheric Sciences*, *62*(12), 4273–4292. https://doi.org/10.1175/jas3614.1

Bretherton, C. S., Macvean, M. K., Bechtold, P., Chlond, A., Cotton, W. R., Cuxart, J., et al. (1999). An intercomparison of radiatively driven entrainment and turbulence in a smoke cloud, as simulated by different numerical models. *Quarterly Journal of the Royal Meteorological Society*, *125*(554), 391–423. https://doi.org/10.1002/qj.49712555402

Bryan, G. H., & Morrison, H. (2012). Sensitivity of a simulated squall line to horizontal resolution and parameterization of microphysics. *Monthly Weather Review*, *140*(1), 202–225. https://doi.org/10.1175/mwr-d-11-00046.1

Carpenter, R. L., Droegemeier, K. K., & Blyth, A. M. (1998). Entrainment and detrainment in numerically simulated cumulus congestus clouds. Part I: General results. *Journal of the Atmospheric Sciences*, *55*(23), 3417–3432. https://doi.org/10.1175/1520-0469(1998)055<3417:eadins>2.0.co;2

Carstens, J. D., & Wing, A. A. (2022). A spectrum of convective self-aggregation based on background rotation. *Journal of Advances in Modeling Earth Systems*, *14*(5), e2021MS002860. https://doi.org/10.1029/2021ms002860

Chen, Y.-T., & Wu, C.-M. (2019). The role of interactive SST in the cloud-resolving simulations of aggregated convection. *Journal of Advances in Modeling Earth Systems*, *11*(10), 3321–3340. https://doi.org/10.1029/2019ms001762

Clough, S. A., Shephard, M. W., Mlawer, E. J., Delamere, J. S., Iacono, M. J., Cady-Pereira, K., et al. (2005). Atmospheric radiative transfer modeling: A summary of the AER codes. *Journal of Quantitative Spectroscopy and Radiative Transfer*, *91*(2), 233–244. https://doi.org/10.1016/j.jqsrt.2004.05.058

Coppin, D., & Bony, S. (2015). Physical mechanisms controlling the initiation of convective self-aggregation in a general circulation model. *Journal of Advances in Modeling Earth Systems*, *7*(4), 2060–2078. https://doi.org/10.1002/2015ms000571

Derbyshire, S. H., Beau, I., Bechtold, P., Grandpeix, J.-Y., Piriou, J.-M., Redelsperger, J.-L., & Soares, P. M. M. (2004). Sensitivity of moist convection to environmental humidity. *Quarterly Journal of the Royal Meteorological Society*, *130*(604), 3055–3079. https://doi.org/10.1256/qj.03.130

Grant, L. D., & van den Heever, S. C. (2016). Cold pool dissipation. *Journal of Geophysical Research: Atmosphere*, *121*(3), 1138–1155. https://doi.org/10.1002/2015jd023813

Gu, Y., Liou, K. N., Ou, S. C., & Fovell, R. (2011). Cirrus cloud simulations using WRF with improved radiation parameterization and increased vertical resolution. *Journal of Geophysical Research*, *116*(D6), D06119. https://doi.org/10.1029/2010jd014574

Guo, Liu, Daum, Zeng, Li, & others (2008). Effects of model resolution on entrainment (inversion heights), cloud-radiation interactions, and cloud radiative forcing. *Chemistry and Physics of Lipids*.

Held, I. M., Hemler, R. S., & Ramaswamy, V. (1993). Radiative-convective equilibrium with explicit two-dimensional moist convection. *Journal of the Atmospheric Sciences*, *50*(23), 3909–3927. https://doi.org/10.1175/1520-0469(1993)050<3909:rcewet>2.0.co;2

Holloway, C. E., & Neelin, J. D. (2009). Moisture vertical structure, column water vapor, and tropical deep convection. *Journal of the Atmospheric Sciences*, *66*(6), 1665–1683. https://doi.org/10.1175/2008jas2806.1

Holloway, C. E., & Woolnough, S. J. (2016). The sensitivity of convective aggregation to diabatic processes in idealized radiative-convective equilibrium simulations. *Journal of Advances in Modeling Earth Systems*, *8*(1), 166–195. https://doi.org/10.1002/2015ms000511

Huang, J.-d., & Wu, C.-M. (2022). A framework to evaluate convective aggregation: Examples with different microphysics schemes. *Journal of Geophysical Research*, *127*(5), e2021JD035886. https://doi.org/10.1029/2021jd035886

Inness, P. M., Slingo, J. M., Woolnough, S. J., Neale, R. B., & Pope, V. D. (2001). Organization of tropical convection in a GCM with varying vertical resolution; implications for the simulation of the Madden-Julian oscillation. *Climate Dynamics*, *17*(10), 777–793. https://doi.org/10.1007/s003820000148

Jeevanjee, N., & Romps, D. M. (2013). Convective self-aggregation, cold pools, and domain size. *Geophysical Research Letters*, *40*(5), 994–998. https://doi.org/10.1002/grl.50204

Jeevanjee, N., & Zhou, L. (2022). On the resolution-dependence of anvil cloud fraction and precipitation efficiency in radiative-convective equilibrium. *Journal of Advances in Modeling Earth Systems*, *14*(3), e2021MS002759. https://doi.org/10.1029/2021ms002759

Jenney, A. (2023). ajenney/conv_agg_vres_public [Software]. GITHUB. https://github.com/ajenney/conv_agg_vres_public

Khairoutdinov, M. (2022). System for atmospheric modeling (version 6.10.9) [Software]. SAM. http://rossby.msrc.sunysb.edu/~marat/SAM/

Khairoutdinov, M., Krueger, S. K., Moeng, C.-H., Bogenschutz, P. A., & Randall, D. A. (2009). Large-eddy simulation of maritime deep tropical convection. *Journal of Advances in Modeling Earth Systems*, *2*(15), 15. https://doi.org/10.3894/james.2009.1.15

Khairoutdinov, M., & Randall, D. A. (2003). Cloud resolving modeling of the ARM summer 1997 IOP: Model formulation, results, uncertainties, and sensitivities. *Journal of the Atmospheric Sciences*, *60*(4), 607–625. https://doi.org/10.1175/1520-0469(2003)060<0607:crmota>2.0.co;2

Kuang, Z., & Bretherton, C. S. (2006). A Mass-Flux scheme view of a High-Resolution simulation of a transition from shallow to deep cumulus convection. *Journal of the Atmospheric Sciences*, *63*(7), 1895–1909. https://doi.org/10.1175/jas3723.1

Lee, E., Lee, E.-H., & Choi, I.-J. (2019). Impact of increased vertical resolution on Medium-Range forecasts in a global atmospheric model. *Monthly Weather Review*, *147*(11), 4091–4106. https://doi.org/10.1175/mwr-d-18-0387.1

Mackie, A., & Byrne, M. P. (2023). Effects of circulation on tropical cloud feedbacks in high-resolution simulations. *Journal of Advances in Modeling Earth Systems*, *15*(5), e2022MS003516. https://doi.org/10.1029/2022ms003516

Marchand, R., & Ackerman, T. (2010). An analysis of cloud cover in multiscale modeling framework global climate model simulations using 4 and 1 km horizontal grids. *Journal of Geophysical Research*, *115*(D16), D16207. https://doi.org/10.1029/2009jd013423

Matsugishi, S., & Satoh, M. (2022). Sensitivity of the horizontal scale of convective self-aggregation to sea surface temperature in radiative convective equilibrium experiments using a global nonhydrostatic model. *Journal of Advances in Modeling Earth Systems*, *14*(5), e2021MS002636. https://doi.org/10.1029/2021ms002636

Mlawer, E. J., Taubman, S. J., Brown, P. D., Iacono, M. J., & Clough, S. A. (1997). Radiative transfer for inhomogeneous atmospheres: RRTM, a validated correlated-k model for the longwave. *Journal of Geophysical Research*, *102*(D14), 16663–16682. https://doi.org/10.1029/97jd00237

Molinari, J., Romps, D. M., Vollaro, D., & Nguyen, L. (2012). CAPE in tropical cyclones. *Journal of the Atmospheric Sciences*, *69*(8), 2452–2463. https://doi.org/10.1175/jas-d-11-0254.1

Muller, C., & Bony, S. (2015). What favors convective aggregation and why? *Geophysical Research Letters*, *42*(13), 5626–5634. https://doi.org/10.1002/2015gl064260

Muller, C., & Held, I. M. (2012). Detailed investigation of the Self-Aggregation of convection in Cloud-Resolving simulations. *Journal of the Atmospheric Sciences*, *69*(8), 2551–2565. https://doi.org/10.1175/jas-d-11-0257.1

Ohno, T., & Satoh, M. (2018). Roles of cloud microphysics on cloud responses to sea surface temperatures in radiative-convective equilibrium experiments using a high-resolution global nonhydrostatic model. *Journal of Advances in Modeling Earth Systems*, *10*(8), 1970–1989. https://doi.org/10.1029/2018ms001386

Ohno, T., Satoh, M., & Noda, A. (2019). Fine vertical resolution radiative-convective equilibrium experiments: Roles of turbulent mixing on the high-cloud response to sea surface temperatures. *Journal of Advances in Modeling Earth Systems*, *11*(6), 1637–1654. https://doi.org/10.1029/2019ms001704

Parishani, H., Pritchard, M. S., Bretherton, C. S., Wyant, M. C., & Khairoutdinov, M. (2017). Toward low-cloud-permitting cloud superparameterization with explicit boundary layer turbulence: Low-cloud ultraparameterization. *Journal of Advances in Modeling Earth Systems*, *9*(3), 1542–1571. https://doi.org/10.1002/2017ms000968

Patrizio, C. R., & Randall, D. A. (2019). Sensitivity of convective self-aggregation to domain size. *Journal of Advances in Modeling Earth Systems*, *11*(7), 1995–2019. https://doi.org/10.1029/2019ms001672

Pauluis, O., & Garner, S. (2006). Sensitivity of Radiative–Convective equilibrium simulations to horizontal resolution. *Journal of the Atmospheric Sciences*, *63*(7), 1910–1923. https://doi.org/10.1175/jas3705.1

Retsch, M. H., Hohenegger, C., & Stevens, B. (2017). Vertical resolution refinement in an aqua-planet and its effect on the ITCZ. *Journal of Advances in Modeling Earth Systems*, *9*(6), 2425–2436. https://doi.org/10.1002/2017ms001010

Roeckner, E., Brokopf, R., Esch, M., Giorgetta, M., Hagemann, S., Kornblueh, L., et al. (2006). Sensitivity of simulated climate to horizontal and vertical resolution in the ECHAM5 atmosphere model. *Journal of Climate*, *19*(16), 3771–3791. https://doi.org/10.1175/jcli3824.1

Romps, D. M. (2014). An analytical model for tropical relative humidity. *Journal of Climate*, *27*(19), 7432–7449. https://doi.org/10.1175/jcli-d-14-00255.1

Romps, D. M., & Kuang, Z. (2010). Do undiluted convective plumes exist in the upper tropical troposphere? *Journal of the Atmospheric Sciences*, *67*(2), 468–484. https://doi.org/10.1175/2009jas3184.1

Schulz, H., & Stevens, B. (2018). Observing the tropical atmosphere in moisture space. *Journal of the Atmospheric Sciences*, *75*(10), 3313–3330. https://doi.org/10.1175/jas-d-17-0375.1

Seeley, J. T., Jeevanjee, N., Langhans, W., & Romps, D. M. (2019). Formation of tropical anvil clouds by slow evaporation. *Geophysical Research Letters*, *46*(1), 492–501. https://doi.org/10.1029/2018gl080747

Seiki, T., Kodama, C., Satoh, M., Hashino, T., Hagihara, Y., & Okamoto, H. (2015). Vertical grid spacing necessary for simulating tropical cirrus clouds with a high-resolution atmospheric general circulation model. *Geophysical Research Letters*, *42*(10), 4150–4157. https://doi.org/10.1002/2015gl064282

Singh, M. S., & O'Gorman, P. A. (2013). Influence of entrainment on the thermal stratification in simulations of radiative-convective equilibrium. *Geophysical Research Letters*, *40*(16), 4398–4403. https://doi.org/10.1002/grl.50796

Singh, M. S., & O'Gorman, P. A. (2015). Increases in moist-convective updraught velocities with warming in radiative-convective equilibrium: Increases in updraught velocities with warming. *Quarterly Journal of the Royal Meteorological Society*, *141*(692), 2828–2838. https://doi.org/10.1002/qj.2567

Singh, M. S., Warren, R. A., & Jakob, C. (2019). A steady-state model for the relationship between humidity, instability, and precipitation in the tropics. *Journal of Advances in Modeling Earth Systems*, *11*(12), 3973–3994. https://doi.org/10.1029/2019ms001686

Sokol, A. B., & Hartmann, D. L. (2022). Congestus mode invigoration by convective aggregation in simulations of radiative-convective equilibrium. *Journal of Advances in Modeling Earth Systems*, *14*(7), e2022MS003045. https://doi.org/10.1029/2022ms003045

Stevens, B., Lenschow, D. H., Faloona, I., Moeng, C.-H., Lilly, D. K., Blomquist, B., et al. (2003). On entrainment rates in nocturnal marine stratocumulus. *Quarterly Journal of the Royal Meteorological Society*, *129*(595), 3469–3493. https://doi.org/10.1256/qj.02.202

Stevens, B., Moeng, C.-H., Ackerman, A. S., Bretherton, C. S., Chlond, A., de Roode, S., et al. (2005). Evaluation of large-eddy simulations via observations of nocturnal marine stratocumulus. *Monthly Weather Review*, *133*(6), 1443–1462. https://doi.org/10.1175/mwr2930.1

Tobin, I., Bony, S., & Roca, R. (2012). Observational evidence for relationships between the degree of aggregation of deep convection, water vapor, surface fluxes, and radiation. *Journal of Climate*, *25*(20), 6885–6904. https://doi.org/10.1175/jcli-d-11-00258.1

Tompkins, A. M., & Craig, G. C. (1998). Radiative–convective equilibrium in a three-dimensional cloud-ensemble model. *Quarterly Journal of the Royal Meteorological Society*, *124*(550), 2073–2097. https://doi.org/10.1002/qj.49712455013

Tompkins, A. M., & Emanuel, K. A. (2000). The vertical resolution sensitivity of simulated equilibrium temperature and water-vapour profiles. *Quarterly Journal of the Royal Meteorological Society*, *126*(565), 1219–1238. https://doi.org/10.1002/qj.49712656502

Tompkins, A. M., & Semie, A. G. (2017). Organization of tropical convection in low vertical wind shears: Role of updraft entrainment. *Journal of Advances in Modeling Earth Systems*, *9*(2), 1046–1068. https://doi.org/10.1002/2016ms000802

Towns, J., Cockerill, T., Dahan, M., Foster, I., Gaither, K., Grimshaw, A., et al. (2014). XSEDE: Accelerating scientific discovery. *Computing in Science & Engineering*, *16*(5), 62–74. https://doi.org/10.1109/mcse.2014.80

Wang, X., Zhang, G. J., & Wang, Y. (2022). Evaluating and improving scale-awareness of a convective parameterization closure using cloud-resolving model simulations of convection. *Journal of Geophysical Research*, *127*(2), e2021JD035729. https://doi.org/10.1029/2021jd035729

Wing, A. A., & Cronin, T. W. (2016). Self-aggregation of convection in long channel geometry. *Quarterly Journal of the Royal*, *142*(694), 1–15. https://doi.org/10.1002/qj.2628

Wing, A. A., Emanuel, K., Holloway, C. E., & Muller, C. (2017). Convective self-aggregation in numerical simulations: A review. *Surveys in Geophysics*, *38*(6), 1173–1197. https://doi.org/10.1007/s10712-017-9408-4

Wing, A. A., & Emanuel, K. A. (2014). Physical mechanisms controlling self-aggregation of convection in idealized numerical modeling simulations: Self-aggregation mechanisms. *Journal of Advances in Modeling Earth Systems*, *6*(1), 59–74. https://doi.org/10.1002/2013ms000269

Wing, A. A., Reed, K. A., Satoh, M., Stevens, B., Bony, S., & Ohno, T. (2018). Radiative–convective equilibrium model intercomparison project. *Geoscientific Model Development*, *11*(2), 793–813. https://doi.org/10.5194/gmd-11-793-2018

Wing, A. A., Stauffer, C. L., Becker, T., Reed, K. A., Ahn, M., Arnold, N. P., et al. (2020). Clouds and convective Self-Aggregation in a Multi-Model ensemble of Radiative-Convective equilibrium simulations. *Journal of Advances in Modeling Earth Systems*, *12*(9), e2020MS002138. https://doi.org/10.1029/2020ms002138

Yanase, T., Nishizawa, S., Miura, H., Takemi, T., & Tomita, H. (2020). New critical length for the onset of self-aggregation of moist convection. *Geophysical Research Letters*, *47*(16), e2020GL088763. https://doi.org/10.1029/2020gl088763

Zipser, E. J. (2003). Some views on "hot towers" after 50 years of tropical field programs and two years of TRMM data. In W.-K. Tao & R. Adler (Eds.), *Cloud systems, hurricanes, and the tropical rainfall measuring mission (TRMM): A tribute to Dr. Joanne Simpson* (pp. 49–58). American Meteorological Society.